https://dx.doi.org/10.1016/j.isprsjprs.2021.08.003

Improving the accuracy of spring phenology detection by optimally smoothing satellite vegetation index time series based on local cloud frequency

Jiaqi Tian[1], Xiaolin Zhu[1,2*], Jin Chen[3], Cong Wang[4,5], Miaogen Shen[3], Wei Yang[6], Xiaoyue Tan[1], Shuai Xu[1], Zhilin Li[7]

1. Department of Land Surveying and Geo-Informatics, The Hong Kong Polytechnic University, Hong Kong, China
2. Research Institute for Sustainable Urban Development, The Hong Kong Polytechnic University, Hong Kong, China
3. State Key Laboratory of Earth Surface Processes and Resource Ecology, Faculty of Geographical Science, Beijing Normal University, Beijing 100875, China
4. Key Laboratory of Agricultural Remote Sensing (AGRIRS), Ministry of Agriculture and Rural Affairs, Beijing 100081, China
5. Institute of Agricultural Resources and Regional Planning, Chinese Academy of Agricultural Sciences, Beijing 100081, China
6. Center for Environmental Remote Sensing, Chiba University, Chiba 263-8522, Japan
7. Faculty of Geosciences and Environment Engineering, Southwest Jiaotong University, Chengdu 611756, China

*Corresponding author:
Xiaolin Zhu
Address: The Hong Kong Polytechnic University, Room ZS621, Block Z, 181 Chatham Road South, Kowloon, Hong Kong.
Phone: +852-2766-5976; Email: xiaolin.zhu@polyu.edu.hk

Abstract

Vegetation phenology can be extracted from vegetation index (VI) time series of satellite data. The maximum value composite (MVC) procedure and smoothing filters have been conventionally used as standard methods to exclude noises in the VI time series before extracting the vegetation phenology [e.g., National Aeronautics and Space Administration (NASA) VNP22Q2 and United States Geological Survey (USGS) MCD12Q2 phenology products]. However, it is unclear how to optimize the MVC and smoothing filters to produce the most accurate phenology metrics given that cloud frequency varies spatially. This study designed two simulation experiments, namely (1) using only the MVC and (2) using the MVC and smoothing filters together to smooth the enhanced vegetation index (EVI) time series for detecting spring phenology, i.e., start of season (SOS), over the northern hemisphere (north of 30°N) on a 5° × 5° grid cell basis by the inflection point and relative threshold algorithms. The results revealed that (1) the inappropriate selection of MVC periods (e.g., too short or too long) affected the accuracy of the SOS extracted by both phenology detection algorithms; (2) a filtering process with optimal parameters can reduce the effects of the MVC period on SOS extraction to a considerable extent, i.e., 65% and 61% for iterative Savitzky–Golay (SG) and penalized cubic splines (SP) filters, respectively; (3) optimal parameters for both the MVC and smoothing filters showed significant spatial heterogeneity; and (4) validation with ground PhenoCam data indicated that optimal parameters of the MVC and smoothing filters can produce more accurate results than official vegetation phenology products that use uniform parameters. Specifically, the R^2 values of the NASA product and the USGS product were 0.58 and 0.67, which were increased to 0.70 and 0.81, respectively, by the optimal smoothing process. Optimal parameters of the MVC and smoothing filters provided by this study in each 5° × 5° sub-region may help future studies to improve the accuracy of phenology detection from satellite VI time series.

Key words: maximum value composite; smoothing filter; enhanced vegetation index; spring phenology; start of season

1 Introduction

A shift in the timing of vegetation phenology, particularly for spring phenology, i.e., the start of season (SOS), is a critical fingerprint of ecological feedbacks to climate and temperature changes (Fu et al., 2014; Myneni et al., 1997; Shen et al., 2020). In recent decades, with the advantages of the large spatial coverage and multi-year consecutive observations, satellite-derived vegetation indexes (VIs), e.g., the normalized difference vegetation index (NDVI), enhanced vegetation index (EVI), two-band enhanced vegetation index (EVI2), and normalized difference phenology index (NDPI), which record the vegetation growth trajectory, have served as primary data sources for detecting large-scale vegetation phenological metrics (Vrieling et al., 2019; Wang et al., 2017; Zhang et al., 2017; Zhou et al., 2016). However, the raw daily VI time series has noises caused by cloud contamination and atmospheric conditions. To exclude the noises, the maximum value composite (MVC) procedure and smoothing filters have been conventionally used as standard smoothing procedures (Figure 1) to preprocess raw VI data from daily satellite data [e.g., Moderate Resolution Imaging Spectroradiometer (MODIS), Advanced Very High Resolution Radiometer (AVHRR), Satellite Pour 1'Observation de la Terre (SPOT), and Visible Infrared Imaging Radiometer Suite (VIIRS)] before extracting the vegetation phenology (Buitenwerf et al., 2015; Cong et al., 2012; White et al., 2009).

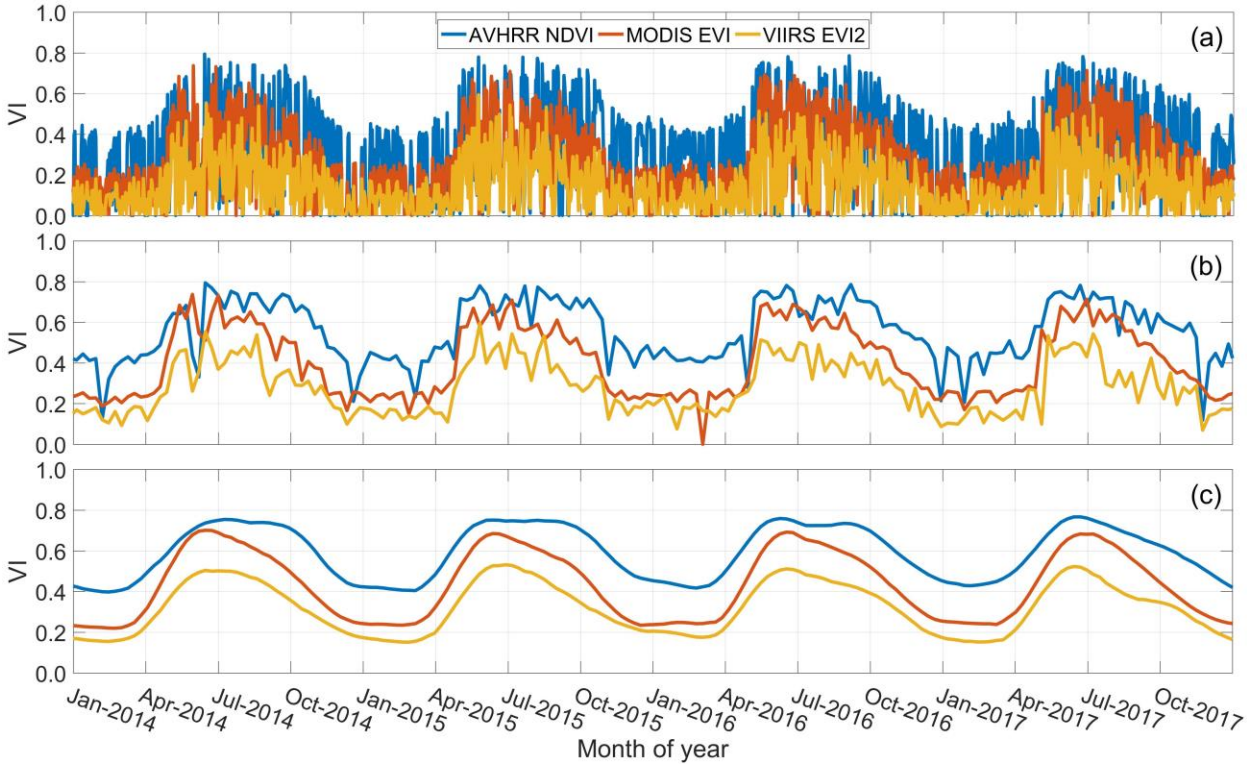

Figure 1. Example of the smoothing process for a raw daily vegetation index (VI) time series (a) to a composited VI time series with an 8-day composite period by the maximum value composite (MVC) procedure (b) and a smoothed VI time series by the iterative Savitzky–Golay (SG) filter (c). The Advanced Very High Resolution Radiometer normalized difference vegetation index (AVHRR NDVI), Moderate Resolution Imaging Spectroradiometer enhanced vegetation index (MODIS EVI), and Visible Infrared Imaging Radiometer Suite two-band enhanced vegetation index (VIIRS EVI2) time series of a deciduous forest pixel (35.79°N, 75.90°W) during 2014–2017 were derived from the AVHRR Surface Reflectance, MODIS MOD09GA, and VIIRS VNP09GA products, respectively.

The MVC procedure selects the maximum VI value from a defined composite period (e.g., 3 to 30 days) to represent the vegetation status for that period in the time series. It assumes that clouds and atmospheric conditions lower the VI values (Figure 1 (a) and (b)) (Holben, 1986; Maisongrande et al., 2004). In the MVC process, the composite period is an important parameter that controls the smoothness of the composited time series. The smoothing filters, such as curve filters (Cao et al., 2018; Chen et al., 2004), fitting functions (Buitenwerf et al., 2015; Julien and Sobrino, 2010; Zhang et al., 2003), convex quadratic model (Beurs and Henebry, 2004), and

moving average or median (Reed et al., 1994) are used to further suppress the noises in the composited VI time series (Figure 1 (c)). In each of these filters, some parameters are used to control the smoothness of the results, such as the smoothing parameter "spar" in the R language of the smoothing spline filter. Most studies on vegetation phenology from satellite-based VI time series at large scales used global constant parameters of the MVC and smoothing filters. For example, two official phenology products, namely the National Aeronautics and Space Administration (NASA) Phenology Product (VNP22Q2) and United States Geological Survey (USGS) Land Cover Dynamics Product (MCD12Q2), were derived from the VIIRS MVC-composited 3-day EVI2 and MODIS MVC-composited 5-day EVI2, respectively (Moon et al., 2019).

Although the smoothing process can reduce noisy data in the raw VI time series (Figure 1), it may cause the time series to be over-smoothed and distorted if the technologies are inappropriately used. Several studies explored the effects of composite periods on phenology extraction from VI time series. For instance, a recent study (Zhu et al., 2019) compared the phenological extraction results from two NDVI composites with composite periods of 8 days and 16 days, revealing that the SOS retrieved from the fine composite period was later than that of a coarse composite period. Two other studies indicated that it is more appropriate to use sub-sampled VI composites, i.e., 6 to 16 days (Zhang et al., 2009) and less than 28 days (Kross et al., 2011), if the daily data are of poor quality. Unfortunately, their findings and suggestions may not apply to all regions in the northern hemisphere (north of 30°N) given that cloud frequency is spatially heterogeneous (Figure 2). It shows a glyph-map (Wickham et al., 2012) with spatial cover grid cells of 5° × 5°, demonstrating high temporal variations in cloud coverage ratios. According to the existing study (Wilson and Jetz, 2016), the clouds have a large spatial heterogeneity at large scales, but in small scales, e.g., 5° × 5° grid cell, the cloud cover is relatively homogenous. Figure 2 indicates that using a globally uniform MVC period may be inappropriate to detect the SOS, as composite periods that are too long may lose some information on the changes in natural vegetation greenness, whereas periods that are too short cannot eliminate the noise effects from clouds and the atmosphere, thereby requiring further filtering processes. The differences in both the cloud frequency and MVC period require filtering to change accordingly. Figure 2 illustrates that the cloud coverage varies by month and region

over the northern hemisphere. Therefore, the optimal parameters of the MVC and smoothing filters could be region-dependent rather than globally constant. Existing phenology products (e.g., NASA VNP22Q2 and USGS MCD12Q2) using global constant parameters of the MVC and smoothing filters, i.e., the iterative Savitzky–Golay (SG) filter for NASA and penalized cubic splines (SP) filter for the USGS, might have large uncertainties due to the inaccurate construction of smoothed VI time series. However, there are no guidelines or references on how to set the parameter values in the smoothing steps to obtain the most accurate phenology results. Thus, it is necessary to optimize the smoothing steps of satellite-based VI time series for detecting spring phenology at a large scale, e.g., in the northern hemisphere.

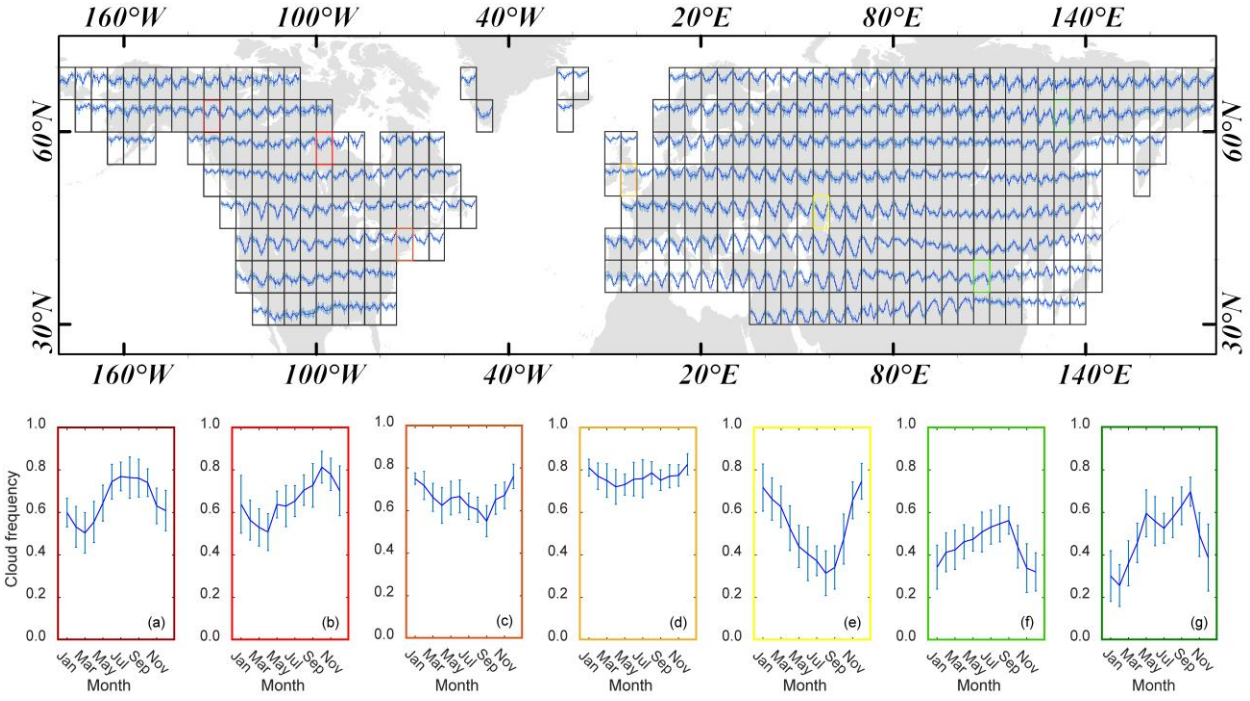

Figure 2. Glyph-map of the average cloud frequency ratio over 20 years from 2000 to 2019 derived from Moderate Resolution Imaging Spectroradiometer (MODIS) MOD09GA. Each grid cell covers a 5° × 5° resolution. (a)–(g) refer to seven distinct regions of cloud coverage, and the color of the box border indicates the location of the regions.

The objectives of this study were (1) to investigate how the MVC periods affect the SOS extraction accuracy over the northern hemisphere, and whether the filtering process (SG and SP filters) can alleviate this effect; and (2) to recommend the optimal parameters of the MVC and

smoothing filters for detecting vegetation spring phenology in different regions over the northern hemisphere. To achieve the objectives, we designed two simulation experiments to optimize the smoothing process of cloudy EVI time series for use of the MVC alone and the combined use of the MVC and filters to extract the SOS. Cloudy EVI curves were first simulated with cloud contamination and noise based on the reference EVI curve and local cloud frequency of each 5° × 5° grid cell, as shown in Figure 2. The parameters of the MVC and smoothing filters were then manipulated to quantify the effects of these parameters on the SOS results. Finally, the optimal parameter values of the MVC and smoothing parameters (SG and SP filters) were proposed for each grid cell.

2 Materials and methods

2.1 EVI time series and cloud frequency

In each 5° × 5° grid cell (Figure 2), the daily-average EVI time series over 20 years from 2000 to 2019 were calculated using three bands [red, blue, and near-infrared (NIR)] of the MODIS Daily Nadir BRDF-Adjusted Reflectance (MCD43A4) product, as shown in Equation (1), and the monthly-average cloud frequencies over 20 years from 2000 to 2019 were extracted from the quality assurance band of the MODIS Terra Surface Reflectance (MOD09GA) product. The 5° × 5° grid cell, which divides each 10° × 10° MODIS tile into four segments, is an appropriate size to study and summarize large-scale phenomena and has been adopted by other studies (Giglio et al., 2018; Wang and Zhu, 2019).

$$EVI = G \times \frac{(NIR - Red)}{(NIR + C_1 \times Red - C_2 \times Blue + L)} \quad (1)$$

where Red, Blue, and NIR refer to the Nadir BRDF-Adjusted Reflectance values in the red, blue, and NIR bands of the MODIS MCD43A4 product. $L = 1$ is the canopy background adjustment, $C_1 = 6.0$ and $C_2 = 7.5$ are the aerosol resistance coefficients, and $G = 2.5$ is the gain factor (Huete et al., 2002, 1994). We focused on the pixels flagged as a vegetation type by the International Geosphere-Biosphere Programme classification scheme of the MODIS Land Cover Type (MCD12Q1) product in 2018, but the barren or sparse vegetation pixels (vegetation cover

< 10%) were excluded to generate the daily-average EVI time series in each grid cell. Because snow cover could depress the VI values, we removed the snow effects using a widely used method (Wang and Zhu, 2019; Zhang, 2015). Specifically, the timing when the land surface temperature extracted from the MODIS MOD11C2 product was less than 278 K was determined as the period of no vegetation activity. The mean of the maximum EVI value during this period in each year from 2000 to 2019 was defined as the background to replace values less than the background value. The EVI was used in this study because: (1) the accuracy of the phenology extracted from the MODIS EVI has been widely validated by field observations (Huete et al., 2002; Zhang et al., 2003), and (2) the EVI can minimize the effects of canopy background signals, and maintain sensitivity to vegetation dynamics and activities (Dallimer et al., 2011). Other satellite-derived VIs (e.g., NDVI, EVI2, and NDPI) may obtain similar results because the cloud effects on these VIs are similar, i.e., clouds decrease the actual VI values.

2.2 MVC method

The MVC procedure is achieved by selecting the highest VI value as the output value of a predefined composite period (e.g., 3 to 30 days) because various types of noise depress the VI values (Holben, 1986; Motohka et al., 2011; Zeng et al., 2020). As a practical and straightforward method, the MVC procedure has generally been used to reconstruct temporally composite VI time series (Table 1) to reduce the noise from clouds, atmosphere, shadows, and viewing and solar angle effects (Wang and Zhu, 2019; Zeng et al., 2020).

Table 1. Studies on vegetation phenology monitoring using the maximum value composite procedure and smoothing filters

Data used	Composite period (days)	Smoothing filter	Extraction method	Reference
MODIS NDVI	30	Polynomial fitting	Relative threshold	(Jeong et al., 2017)
MODIS NDVI	30	Polynomial fitting	Ratio method	(Xu et al., 2020)
MODIS NDVI	16	Multiple methods	Multiple methods	(Zhu et al., 2019)
MODIS NDVI	16	Gaussian function	TIMESAT*[1]	(Zu et al., 2018)
MODIS EVI	16	Logistic function	Inflection point	(Wang et al., 2019)
MODIS EVI	16	Logistic function	TIMESAT	(Zhou et al., 2016)
AVHRR NDVI	15	Multiple methods	Multiple methods	(White et al., 2009)
AVHRR NDVI	15	Cubic spline	Derivatives	(Buitenwerf et al., 2015)
AVHRR NDVI	15	Logistic function	TIMESAT	(He et al., 2017)
AVHRR NDVI	15	BISE*[2]	Ratio method	(Yu et al., 2010)
SPOT NDVI	10	Multiple methods	Multiple methods	(Cong et al., 2012)
SPOT NDVI	10	Multiple methods	Multiple methods	(Bórnez et al., 2020)
SPOT NDVI	10	Multiple methods	Multiple methods	(Delbart et al., 2006)
MODIS EVI	8	Logistic function	Inflection point	(Keenan et al., 2020)
MODIS EVI	8	Logistic function	Inflection point	(Meng et al., 2020)
MODIS EVI2	5	SP filter	Relative threshold	(Moon et al., 2020)
VIIRS EVI2	3	SG filter	Inflection point	(Moon et al., 2019)
MODIS EVI2	3	SG filter	Inflection point	(Wang and Zhang, 2020)
VIIRS EVI2	3	SG filter	Inflection point	(Zhang et al., 2018)
Multiple EVI2*[3]	3	SG filter	Inflection point	(Zhang et al., 2017a)
Fused EVI2*[4]	3	SG filter	Inflection point	(Zhang et al., 2017b)

*[1] TIMESAT is a pixel-based phenology detection toolbox with multiple curve smoothing methods (e.g., Savitzky–Golay filter, asymmetric Gaussian, and double logistic smooth functions) and phenology extraction methods (e.g., absolute and relative threshold methods).

*[2] BISE is the best index slope extraction algorithm, used to reduce the effects of cloud cover, bad atmospheric situations, and bidirectional reflectance on normalized difference vegetation index (NDVI) curves.

*[3] Multiple EVI2 means the two-band enhanced vegetation index (EVI2) derived from the Advanced Very High Resolution Radiometer (AVHRR), Moderate Resolution Imaging Spectroradiometer (MODIS), and Visible Infrared Imaging Radiometer Suite (VIIRS) images.

*[4] Fused EVI2 means the Landsat-MODIS EVI2 fused by the spatiotemporal data fusion algorithm.

SPOT: Satellite Pour l'Observation de la Terre.

2.3 Smoothing filters

Smoothing filters are frequently used to further suppress the noises in the composited VI time series (Table 1). For instance, two official phenology products (VIIRS VNP22Q2 and MODIS MCD12Q2) adopt the SG filter and SP filter, respectively. The original SG filter was proposed to smooth and calculate derivatives of a spectrum or a set of consecutive values by a simplified least-squares-fit convolution (Savitzky and Golay, 1964). Because it has good adaptability to smooth any continuous data at a fixed and uniform interval, some algorithms based on the original SG filter were further developed to smooth satellite-based VI time series, such as the iterative SG filter (Chen et al., 2004) and spatial-temporal SG method (Cao et al., 2018). The SP filter is less robust than some of other smoothing algorithms (e.g., logistic functions) when missing data are prevalent, as it fits data locally, making it more sensitive to gaps and high-frequency changes in VI time series (Zhang et al., 2018). However, the SP filter has greater flexibility than logistic functions to capture a broader dynamic range of VI time series (e.g., asymmetric phenology) (Moon et al., 2019; Verma et al., 2016).

2.4 Phenology extraction method

Two phenology extraction methods (i.e., inflection point and relative threshold) adopted by the NASA and USGS phenology products were used to detect the SOS. The inflection point method identifies the inflection point of the VI time series to define the SOS, whereas the relative threshold method determines the SOS with a predefined percentage of VI amplitude (Shang et al., 2017). For the inflection point method, curve fitting by a four-parameter logistic function as shown in Equation (2), was accomplished before SOS extraction.

$$y(t) = \frac{c}{1 + e^{a+bt}} + d \quad (2)$$

where t is the time on the day of the year, $y(t)$ is the fitted EVI value at date t, a and b are the fitting parameters, $c + d$ is the maximum EVI value, and d is the initial background EVI value. This depiction can be applied to reflect the phenology of ecosystems (Zhang et al., 2003). The

rate of change of curvature (RCC) was then calculated by Equation (3). Finally, the SOS was determined as the time when the RCC reaches its first maximum value (Zhang et al., 2003).

$$RCC = b^3 cz\left\{\frac{3z(1-z)(1+z)^3[2(1+z)^3+b^2c^2z]}{[(1+z)^4+(bcz)^2]^{2.5}} - \frac{(1+z)^2(1+2z-5z^2)}{[(1+z)^4+(bcz)^2]^{1.5}}\right\} \quad (3)$$

where $z = e^{a+bt}$. For the relative threshold method, the SOS was estimated as the date when the VI increased by a predefined threshold (e.g., 10%, 15%, and 20%) of its annual amplitude (Moon et al., 2019; Shang et al., 2017; Shen et al., 2014).

3 Experimental design

3.1 Experiment 1: Optimizing the smoothing process for use of the MVC alone

Step 1: Simulate the daily cloudy EVI time series and composite them using the MVC

Some satellite products can provide MVC-composited VI products, such as MODIS 8-day and 16-day, SPOT 10-day, and AVHRR 15-day VI products, but there are too few composite periods to satisfy the need for a comprehensive study. These VI products derived from different satellite sensors have non-negligible differences in the spatial resolutions, sensor configurations, and atmospheric conditions of image acquisition. Thus, it is challenging to exclusively explore the effects of the parameters of the MVC and smoothing filters on spring phenology detection. To avoid these issues, we first calculated the reference EVI time series (EVI_{ref}), namely the daily-average EVI curves of all vegetation pixels over each 5° × 5° grid cell (Figure 2) over 20 years from 2000 to 2019, as describes in Section 2.1. The EVI_{ref} is a smooth curve representing the average vegetation growth cycle of each grid cell. The MVC-composited EVI time series with a series of composite periods ranging from 3 to 30 days were then generated from the simulated daily EVI time series (EVI_s). The EVI_s in each grid cell were derived from the EVI_{ref} by randomly adding the Gaussian noise effect and local cloud effect, as shown in Equation (4):

$$EVI_s = EVI_{ref} + \varepsilon + \delta \quad (4)$$

where ε and δ refer to the Gaussian noise effect and cloud effect, respectively. We first added a minor Gaussian noise effect [mean: 0; standard deviation (std): 0.02] into the EVI_{ref} to represent the component of random noise in satellite images (Cao et al., 2015). A certain number of days were then randomly selected as cloudy days according to the local cloud frequency in each grid cell (Figure 3 (a)). Next, the EVI values of the selected cloudy days were randomly lowered by 10% to 100% (Figure 3 (b)) because clouds lower the actual VI values (Motohka et al., 2011). The EVI_s in each grid cell were simulated 1000 times using the above procedures to generate substantial and sufficient samples. Last, in each grid cell, we composited these 1000 simulated daily EVI_s using the MVC with a wide range of composite periods, including 3, 5, 8, 12, 16, 20, 24, and 30 days, as shown in Figure 3 (c). Thus, for each composite period, there were 1000 MVC-composited EVI (EVI_{MVC}) time series in each grid cell.

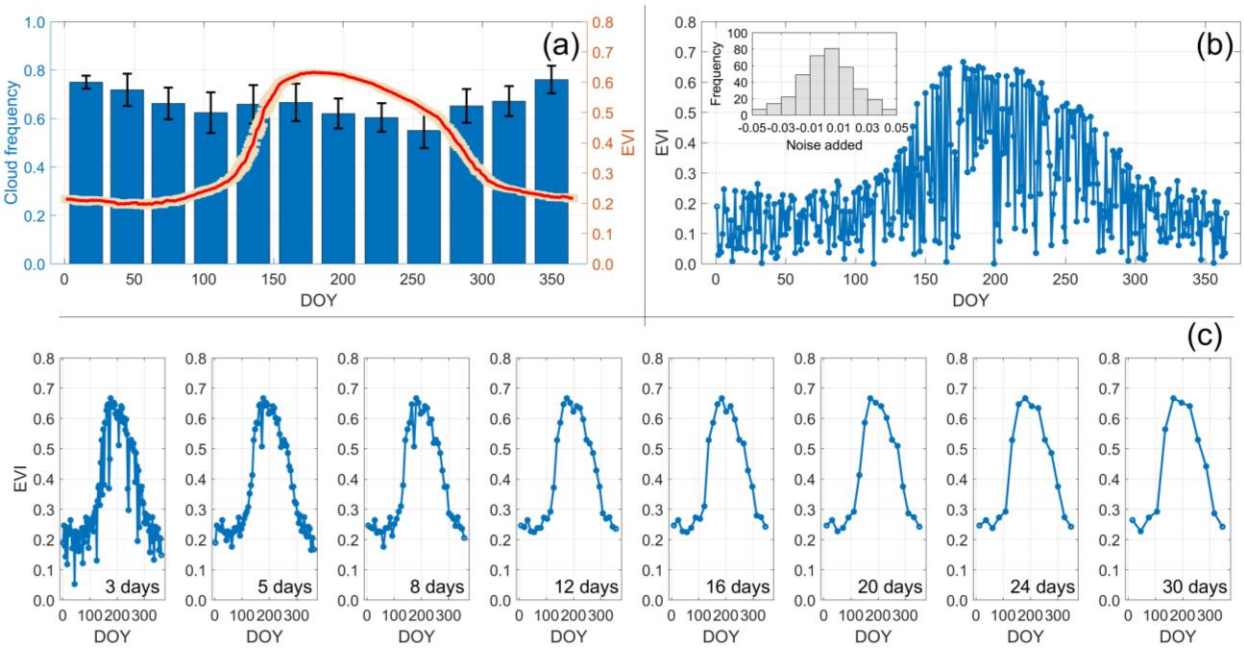

Figure 3. Reference enhanced vegetation index time series (EVI_{ref}) and local monthly-average cloud frequency ratio in a grid cell (central coordinate: 42.50°N, 72.50°W) (a), simulation of daily EVI_s (b), and maximum value composite (MVC)-composited EVI time series of different composite periods from 3 to 30 days (c). DOY: day of year.

Step 2: Extract the SOS using the inflection point and relative threshold methods

We extracted the SOS from the EVI_{MVC} time series at different composite periods by using the inflection point and relative threshold methods, as described in Section 2.4. For the inflection point method, the date of the SOS was defined as when the RCC reaches its local first maximum value. A threshold of 15% was used for the relative threshold method to determine the SOS date according to the threshold adopted by the USGS MCD12Q2 phenology product (Moon et al., 2019). The results from each phenology extraction method were named MVC-inflection and MVC-threshold.

Step 3: Quantify the accuracy of the SOS extraction and determine the optimal MVC period in each grid cell

The SOS values extracted from the EVI_{ref} in each 5° × 5° grid cell (Figure 2) using the inflection point and relative threshold algorithms were used as the "true value" (hereafter named "SOS_{ref}") (see Figure S1 in Appendix A. Supplementary data). The root mean square error (RMSE) and average difference (AD) as Equations (5) and (6), respectively, between the SOS_{ref} and SOS detected from the 1000 simulated EVI time series in each grid cell were then used to quantify the accuracy of the SOS extraction from the EVI_{MVC} time series using different composite periods. The RMSE and AD can be used to measure the spread of error and biasness of the detected SOS, respectively (Zhang et al., 2017b).

$$RMSE = \sqrt{\frac{\sum_{i=1}^{1000}(SOS_{ref} - SOS_i)^2}{1000}} \quad (5)$$

$$AD = \frac{\sum_{i=1}^{1000}(SOS_{ref} - SOS_i)}{1000} \quad (6)$$

After quantifying the accuracy of the SOS extracted by a series of composite periods, we could determine the optimal composite period in each grid cell for future works and the research community. In each grid cell, the composite period with the highest SOS extraction accuracy was considered the optimal period. Therefore, the optimal composite period can best balance the removal of noises and the preservation of temporal information to produce more accurate and reliable SOS results.

3.2 Experiment 2: Optimizing the smoothing process for the combined use of the MVC and filters

For experiment 2 we modified some steps of experiment 1. Specifically, we smoothed the MVC-composited EVI time series by filters with optimal parameters before SOS extraction after generation of the EVI_{MVC} time series (Step 1 in Section 3.1). We utilized two smoothing filters (SG and SP filters) that are used in two official phenology products (VIIRS VNP22Q2 and MODIS MCD12Q2). Previous phenology studies often used default filter parameters, such as a half-window of 4 and a smoothing polynomial of 6 for the SG filter to smooth the 10-day MVC VI time series (Chen et al., 2004) and a smoothing parameter of 0.4 for the SP filter to smooth the 5-day MVC VI time series (Moon et al., 2019). Because this study extracted the SOS from 3-day to 30-day MVC-composited EVI time series, the default filter parameters may not have been applicable to the EVI_{MVC} time series of different composite periods. Thus, we evaluated the accuracy of the smoothing results of different parameters to determine the optimal parameter values. We tested a half-window from 2 to 8 and a smoothing polynomial from 2 to 6 for the SG filter, as well as smoothing parameters from 0.1 to 1.0 with increments of 0.1 for the SP filter. The RMSE between the EVI_{ref} curve and the smoothed EVI_{MVC} curve was used to evaluate the accuracy of the time series smoothed by the SG and SP filters with different parameters. For each filter, the parameter corresponding to the minimal RMSE was determined as the optimal parameter for smoothing the EVI_{MVC} curves. The SOS results were then extracted from the smoothed EVI_{MVC} curves by the inflection point and relative threshold methods (Step 2 in Section 3.1). The results from each phenology extraction method were named MVC-SG-inflection and MVC-SP-threshold, respectively. Finally, the accuracy of the SOS extraction was quantified, which was used to determine the optimal MVC period in each grid cell when filters were applied (Step 3 in Section 3.1).

3.3 Comparison of experiments 1 and 2

It is expected that the short MVC periods (e.g., 3 and 5 days) cannot fully remove the cloud contaminations and noises in the original daily EVI time series as shown in Fig.3(c), especially

in cloudy regions. It makes the accuracy of SOS detection sensitivity to the MVC periods (i.e., composite period effect). In other words, inappropriate MVC periods would greatly lower down the accuracy of SOS detection. The smoothing filters can further remove these residual noises which would reduce the sensitivity of SOS detection to the MVC periods. A comparison of results between experiments 1 and 2 can confirm this assumption. Accordingly, we further calculated the relative difference (RD) of the composite period effect between the results without (i.e., experiment 1) and with the filtering process (i.e., experiment 2), as shown in Equation (7):

$$RD = \frac{SD_1 - SD_2}{SD_1} \times 100\% \quad (7)$$

where SD_1 and SD_2 are the composite period effect without and with the filtering process, respectively, which were quantified by the std (i.e., standard deviation) of the SOS accuracy of different composite periods in each grid cell, i.e., larger *SD* values indicate that different composite periods generated SOSs with larger variations. The *RD* value suggests whether the smoothing filters can offset the effect of the MVC periods.

3.4 Validation with ground data

To assess the reliability of the optimal composite periods recommended by our experiments, we used ground data, i.e., digital photographs from the PhenoCam Network, which are commonly used to detect vegetation phenology and dynamics. Compared with satellite remote sensing images, digital repeat photographs are free of contamination from cloud and atmospheric effects and have extremely high temporal resolutions, and thus have a higher accuracy for monitoring vegetation growth. Therefore, the PhenoCam data are widely used as ground truth to validate the phenological metrics extracted by satellite remote sensing data (Moon et al., 2019; Wang et al., 2017). The PhenoCam data can be downloaded from the website (https://phenocam.sr.unh.edu/webcam/). We used 35 PhenoCam Network sites (Figure S2 in Appendix A. Supplementary data) that were classified into type I sites (i.e., data of the highest quality), including multiple vegetation types: (deciduous broadleaf, evergreen needleleaf, shrub, agriculture, grassland and wetland) (Table S1 in Appendix A. Supplementary data). In the

PhenoCam image processing, the green chromatic coordinate (GCC), which reflected relative brightness, was first calculated using Equation (8), as follows:

$$GCC = \frac{G}{R + G + B} \tag{8}$$

where the parameters *R*, *G*, and *B* refer to the red, green, and blue digital numbers extracted from the regions of interest of the PhenoCam imagery, thereby indicating the relative brightness in these wavelengths. The GCC SOSs were extracted by the inflection point and relative threshold methods, as described in Section 2.4. The GCC SOSs were used as ground truth to assess whether the optimal time series smoothing process can improve the accuracy of SOS detection.

4 Results

4.1 Results of experiment 1

(1) SOS accuracy extracted by different composite periods

Figure 4 shows the spatial distributions of the RMSE of SOS derived from the EVI composites with different composite periods for the use of the MVC alone by the inflection point and relative threshold methods. The results were named MVC-inflection and MVC-threshold, respectively. The results revealed a notable inconsistency of the SOS extraction results (i.e., different spatial distributions of the RMSE of the SOS) when using the MVC-composited EVI with different composite periods regardless of which phenology extraction method was used (Figure 4). Specifically, the RMSE of the SOS for the MVC-inflection and MVC-threshold results generally showed a lower accuracy of SOS extraction when using shorter composite periods (e.g., 3–8 days) compared with longer periods (e.g., 20–30 days).

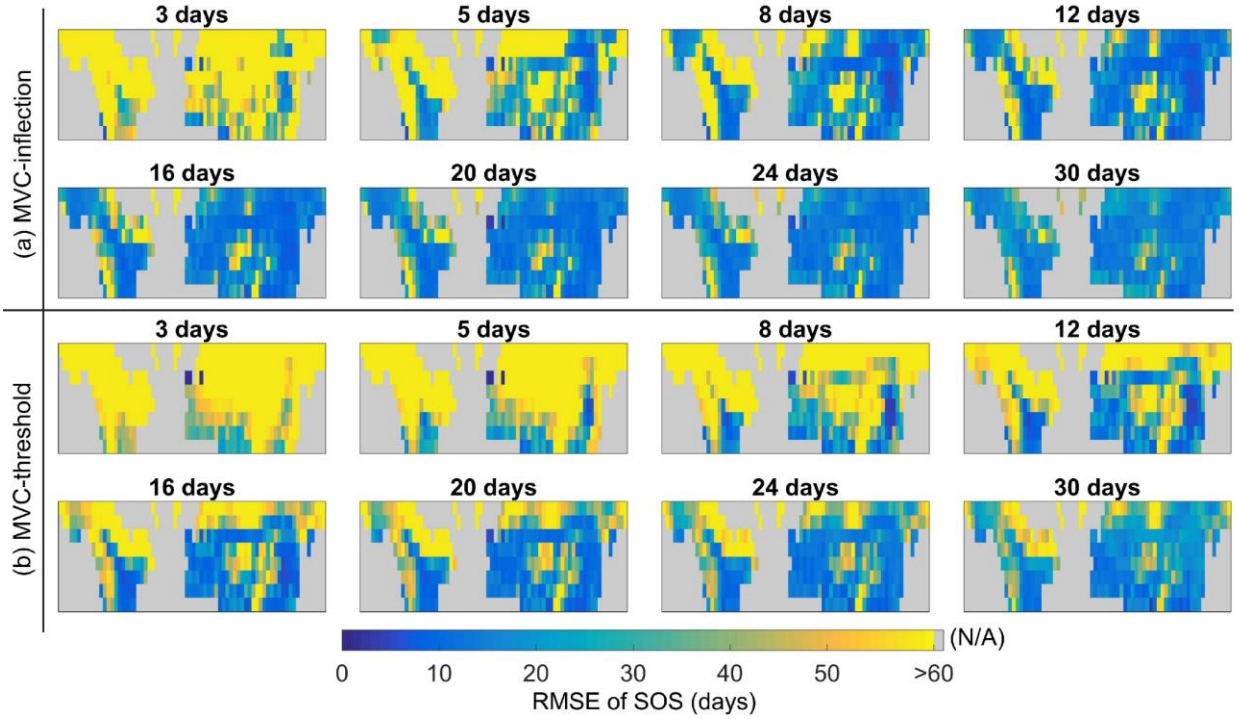

Figure 4. Spatial distributions of the root mean square error (RMSE) of the start of season (SOS) extracted from different composite periods for the use of the maximum value composite (MVC) alone by the inflection point method (a) and relative threshold method (b). Dark blue indicates minimum RMSE (i.e., highest accuracy), and light yellow denotes maximum RMSE (i.e., lowest accuracy).

Although this study adopted two statistical metrics (i.e., RMSE and AD) to qualify the accuracy of SOS detected by a series of composite periods, we found that the results between RMSE and AD have high consistency, as shown in Figure 5. Also, the spatial distributions of the AD of SOS extracted from different composite periods for the use of the MVC alone (Figure S3 in Appendix A. Supplementary data) are similar with that of RMSE. It means that the error of detected SOS was mainly due to a systematic bias for a given composite period. Considering that RMSE is a widely and accepted measure of differences between values predicted and the values observed, we used RMSE to select the optimal composite period in this study.

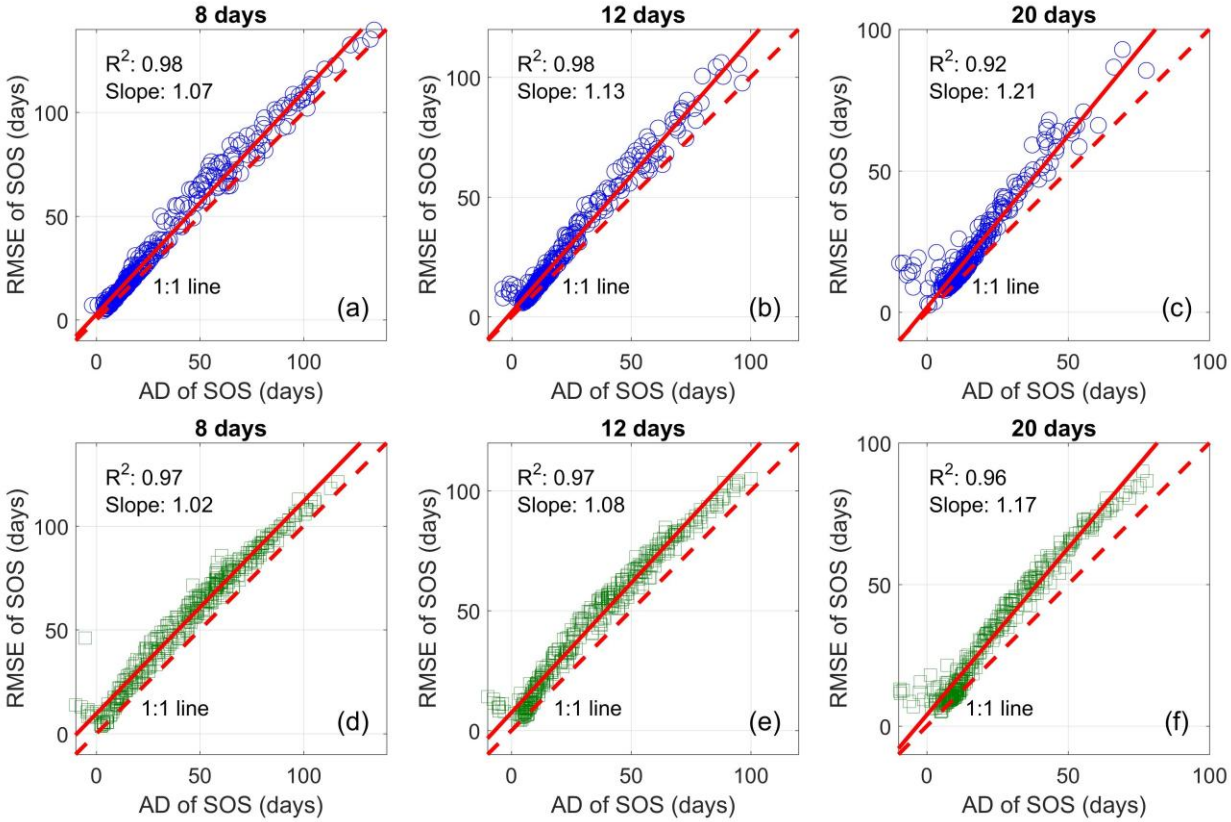

Figure 5. Comparison of accuracy of SOS (i.e., RMSE and AD) extracted by 8-day, 12-day and 20-day EVI time series. (a)–(c) were results of using inflection point method and (d)–(f) using relative threshold method.

(2) Optimal composite period of each grid cell

Figure 6 shows the optimal composite period of each grid cell, which produces the most accurate SOS results, and the spatial patterns of SOS accuracy extracted by the optimal composite period of each grid cell. The optimal composite period of each grid cell showed significant spatial heterogeneity, as shown in Figure 6 (a) and (b). Both phenology extraction methods generally showed that the optimal composite periods were longer (mainly 30 days) if not incorporating the filtering process, as shown in Figure 6 (e) and (f). Moreover, the spatial patterns of SOS accuracy were dominated by dark blue and blue grid cells, as shown in Figure 6 (c) and (d), thereby suggesting that the SOS extraction accuracy was higher than that when using a global uniform composite period (Figure 4).

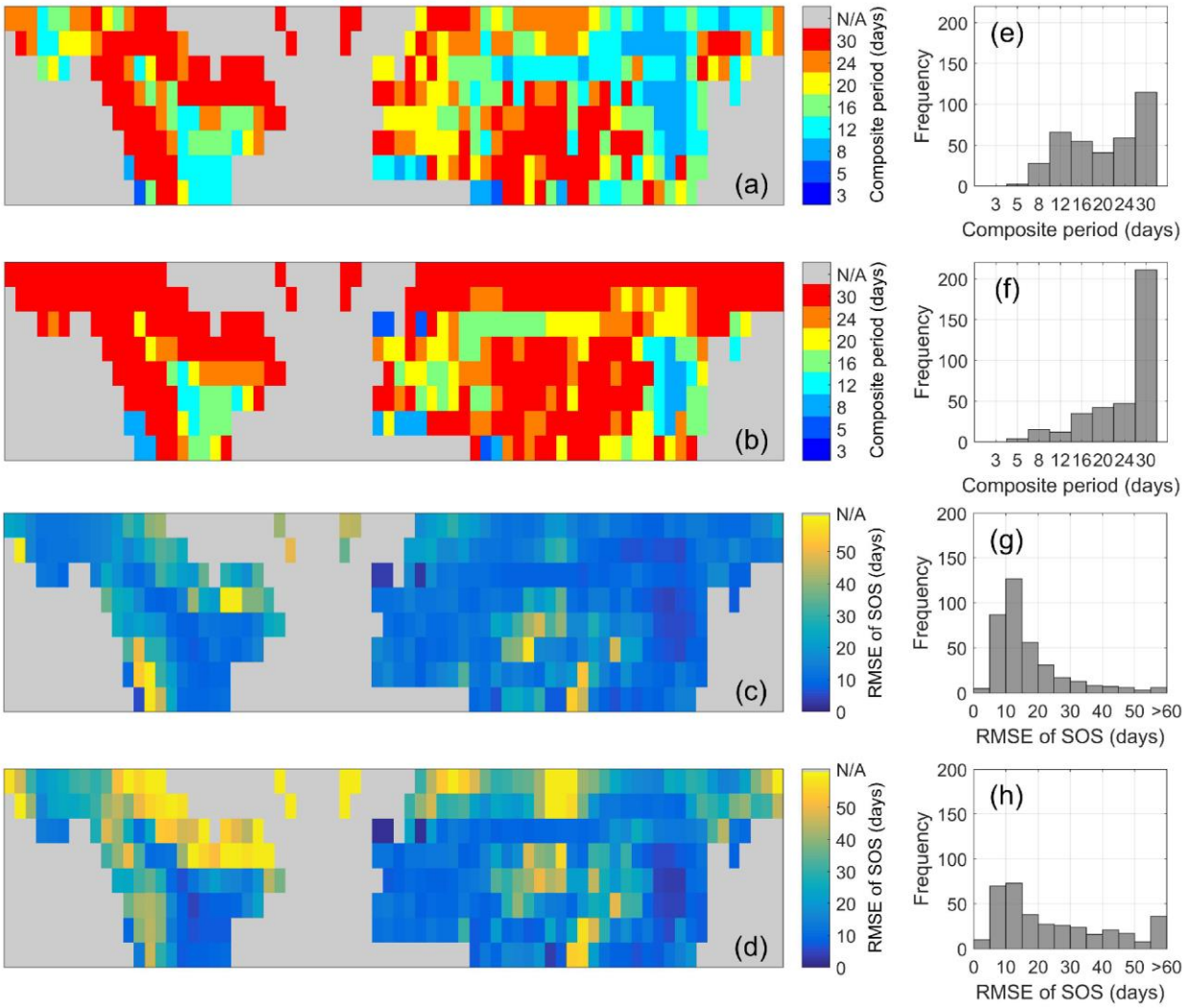

Figure 6. Spatial distributions of the optimal composite periods for maximum value composite (MVC)-inflection (a) and MVC-threshold (b) and spatial distributions of the start of season (SOS) accuracy extracted by the optimal composite period of each grid cell for MVC-inflection (c) and MVC-threshold (d). The histograms summarize the corresponding optimal composite periods and the root mean square error (RMSE) the of SOS.

4.2 Results of experiment 2

(1) Optimal smoothing filter parameters for different composite periods

As shown in Figure 7, the optimal parameters of both the SG and SP filters generally varied by region and composite period, which indicated that using the global constant filter parameter may cause misconstruction of VI time series. For the SG filter, the default parameters (i.e., half-

window of 4 and smoothing polynomial of 6) seemed more suitable for composite periods longer than or equal to 12 days (Figure 7). Moreover, there was evident spatial heterogeneity of the optimal filter parameters when using composite periods shorter than or equal to 8 days, especially 5 days. For the SP filter, as the composite periods became longer, the optimal filter parameters generally became smaller, thereby suggesting that the default parameter (0.4) is not applicable for all composite periods. For instance, the distributions of the optimal SP filter parameters concentrated on larger values (i.e., 0.6 and 0.7) when smoothing 3-day EVI composites, whereas they were smaller (i.e., 0.2 and 0.3) when filtering 30-day EVI composites (Figure 7). In general, the EVI time series resampled into shorter composite periods had greater fluctuations because of cloud and noise effects (Figure 3), so larger SP filter parameters are necessary to reduce fluctuations and smooth curves.

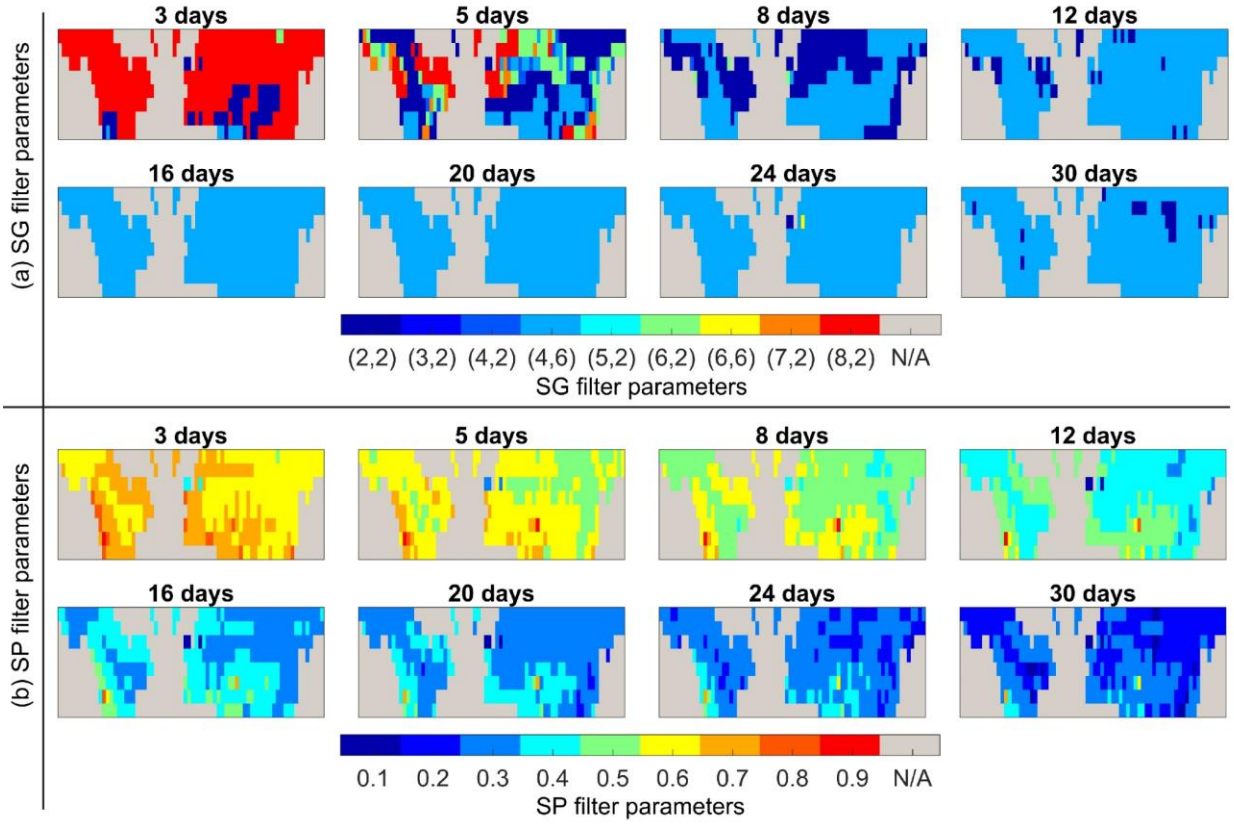

Figure 7. Spatial distributions of the optimal parameters of the iterative Savitzky–Golay (SG) (a) and penalized cubic splines (SP) (b) filters at different composite periods.

(2) SOS accuracy extracted by different composite periods

Figure 8 indicates the spatial distributions of the SOS accuracy derived from the EVI composites with different composite periods for the combined use of the MVC and filters using the inflection point and relative threshold methods. The results were named MVC-SG-inflection and MVC-SP-threshold, respectively. Compared with the results without the filtering process (Figure 4), Figure 8 also shows a clear spatial difference in the accuracy of SOS extraction with the filtering process regardless of the phenology extraction method used. Conversely, the longer composite periods (e.g., 20–30 days) produced less accurate SOS results than short periods (e.g., 3–8 days) for the MVC-SG-inflection and MVC-SP-threshold results (Figure 8).

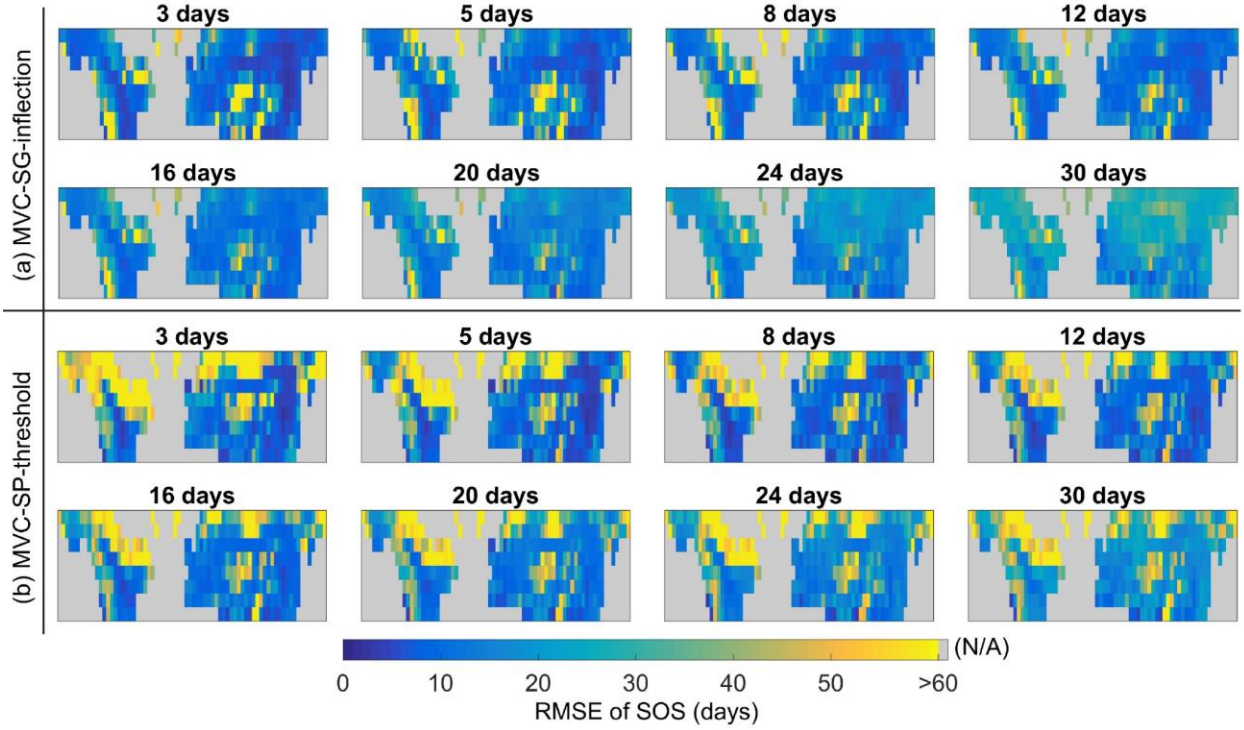

Figure 8. Spatial distributions of the root mean square error (RMSE) of the start of season (SOS) extracted from different composite periods for the combined use of the maximum value composite (MVC) and filters using the inflection point method (a) and relative threshold method (b). SG: iterative Savitzky–Golay; SP: penalized cubic splines.

(3) Optimal composite period of each grid cell

Figure 9 shows the optimal composite period and spatial distributions of SOS accuracy, which were extracted by the optimal composite period using the corresponding optimal filtering parameters (Figure S4 in Appendix A. Supplementary data) for each grid cell. Figure 9 (a) and (b) illustrates that the optimal composite period of each grid cell showed significant spatial heterogeneity, which is a similar finding to the results without the filtering process (Figure 6). However, the optimal composite periods were generally shorter (3 days for the inflection point method and 8 days for the relative threshold method) if incorporating the filtering process, as shown in Figure 9 (e) and (f). The spatial patterns of SOS accuracy extracted by the optimal parameters of the MVC (Figure 9) were dominated by dark blue and blue grid cells, as shown in Figure 9 (c) and (d), thereby suggesting that the SOS extraction accuracy was higher than that using the global uniform composite period (Figure 8).

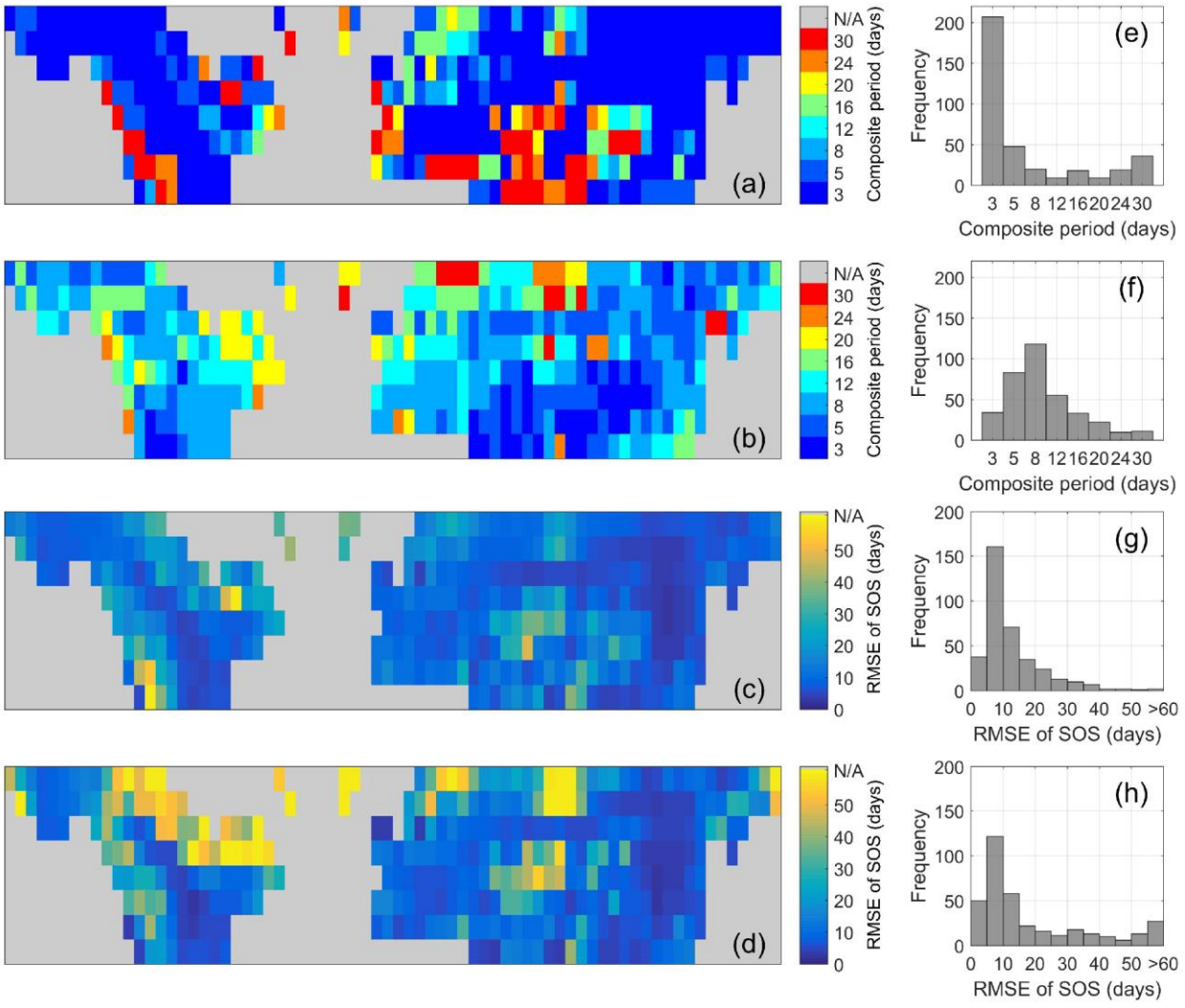

Figure 9. Spatial distributions of the optimal composite periods for the maximum value composite (MVC)-Savitzky–Golay (SG)-inflection (a) and MVC-penalized cubic splines (SP)-threshold (b) and spatial distributions of the start of season (SOS) accuracy extracted by the optimal composite period of each grid cell for the MVC-SG-inflection (c) and MVC-SP-threshold (d). The histograms summarize the corresponding optimal composite periods and the root mean square error (RMSE) of the SOS.

4.3 Comparison of the results of experiments 1 and 2

We further quantified how the filtering process alleviated the effect of the MVC periods on SOS detection. The RD values (described in Section 3.3) of each grid cell are presented in Figure 10. The yellow and yellowish-green regions (i.e., greater positive RD values) dominated most regions over the northern hemisphere, thereby suggesting that the filtering steps can significantly alleviate the effects from the composite periods on SOS detection. On average, 65% and 61% of the effects of the composite periods on SOS extraction were eliminated for the inflection point and relative threshold methods, respectively (Figure 10 (c) and (d)). Overall, the inappropriate MVC-composited periods strongly affected the accuracy of SOS extraction, but the filtering step (SG and SP filters) greatly reduced this effect (Figure 4 and Figure 8).

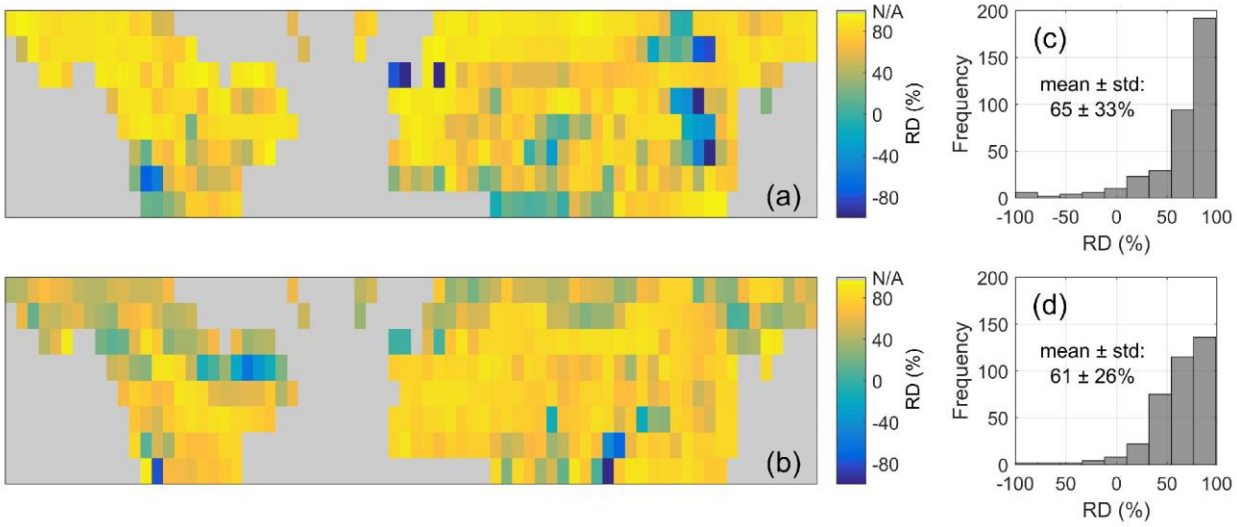

Figure 10. Spatial distributions of the relative difference (RD) derived by the inflection point method (a) and the relative threshold method (b). The histograms summarize the RD values of

509 the inflection point method (c) and the relative threshold method (d). The positive (or negative)
510 RD values refer to the filtering process can reduce (or enlarge) the sensitivity of SOS extraction
511 accuracy to the MVC periods.
512
513 To quantitatively compare the SOS extraction accuracy under different procedures, the statistics
514 (i.e., mean and std) of the RMSE of the SOS derived without filtering (MVC-inflection and
515 MVC-threshold), and with filtering (MVC-SG-inflection and MVC-SP-threshold) experiments
516 are summarized in Table **2**. The statistics include the RMSE of the SOS extracted by eight
517 composite periods from 3 to 30 days and optimal composite periods (Figure 6 and Figure 9). The
518 24-day and 30-day composite periods had the highest accuracy of SOS extraction for the MVC-
519 inflection method (RMSE: 19.42 ± 12.24 days) and MVC-threshold method (RMSE: 27.21 ±
520 15.31 days), respectively. Nevertheless, the composite periods with the highest accuracy of SOS
521 extracted by the MVC-SG-inflection method (16.64 ± 10.99 days) and MVC-SP-threshold
522 method (21.83 ± 19.10 days) were 16 days and 8 days, respectively. Using the grid-based
523 optimal composite period produced SOS results with good accuracy, i.e., the MVC-inflection
524 method (16.97 ± 11.08 days), MVC-threshold method (24.80 ± 17.03 days), MVC-SG-inflection
525 method (12.61 ± 9.41 days), and MVC-SP-threshold method (18.85 ± 17.23 days), as shown in
526 Table 2. The accuracy was higher than that obtained using a globally uniform composite period.
527
528 Table 2. Statistics (mean: $\bar{x}$; and std: σ) for each composite period and optimal composite period

Composite period	RMSE of SOS extracted via the MVC-inflection		RMSE of SOS extracted via the MVC-SG-inflection		RMSE of SOS extracted via the MVC-threshold		RMSE of SOS extracted via the MVC-SP-threshold	
	$\bar{x}$	σ	$\bar{x}$	σ	$\bar{x}$	σ	$\bar{x}$	σ
3	52.32	13.77	16.40	15.66	54.53	10.68	28.80	21.81
5	40.10	19.85	17.71	15.32	51.04	15.21	23.94	20.25
8	28.93	20.26	18.19	15.59	45.60	18.53	**21.83**	19.10
12	23.48	17.98	16.69	12.92	38.85	20.62	22.24	18.46
16	21.05	15.65	**16.64**	10.99	33.81	20.67	24.39	18.73
20	20.22	13.80	17.82	9.42	30.54	19.51	25.13	17.88
24	**19.42**	12.24	19.65	8.19	28.40	17.81	26.72	17.53
30	19.88	9.96	24.41	7.92	**27.21**	15.31	29.10	16.30
Optimal	**16.97**	11.08	**12.61**	9.41	**24.80**	17.03	**18.85**	17.23

529 RMSE: root mean square error; SOS: start of season; MVC: maximum value composite; SG:
530 iterative Savitzky–Golay; SP: penalized cubic splines.
531

To compare the results of the two phenological detection methods more intuitively, the highest accuracy of four conditions (using the uniform composite period or local optimal composite period, with/without the filtering process) is plotted in Figure 11. Two SOS extraction algorithms (inflection point and relative threshold) had similar findings, as followed: (1) the algorithms with and without filtering steps suggested that using local optimal composite periods produced more accurate SOS results than using a globally uniform composite period; (2) regardless of using uniform or optimal composite periods, the filtering steps (SG and SP filters) improved the accuracy of SOS extraction; and (3) the accuracy of the SOS extracted by the inflection point method was generally higher than that of the relative threshold method regardless of the preprocessing steps used.

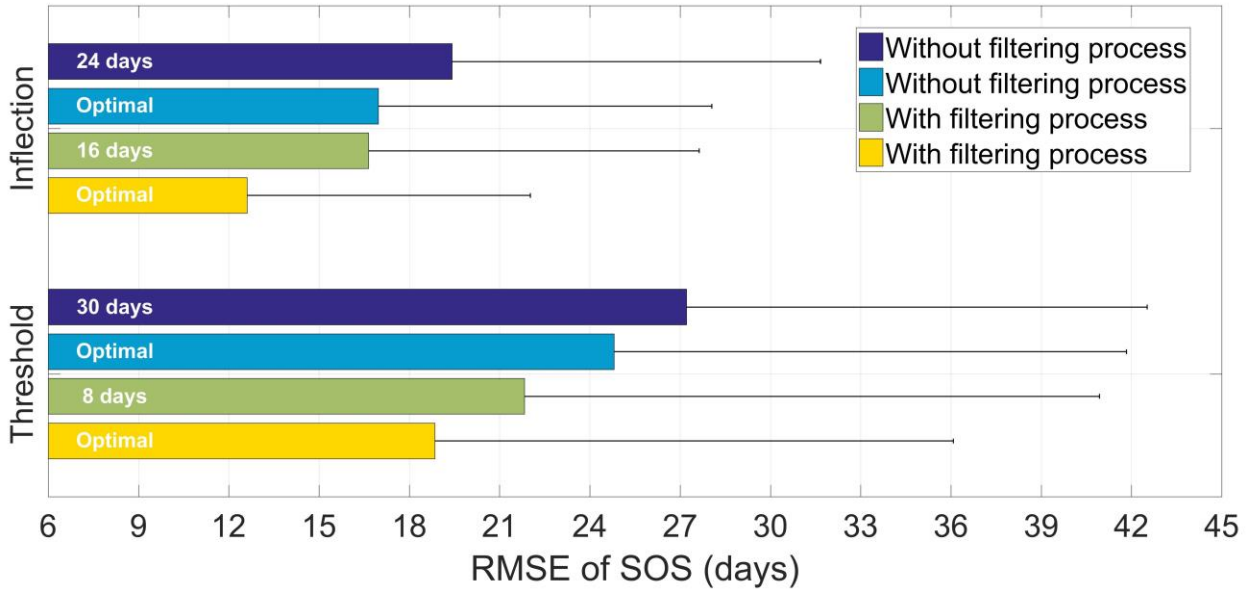

Figure 11. Comparison of the accuracy of the start of season (SOS) extracted by the uniform and optimal composite periods using the inflection point method and relative threshold method. RMSE: root mean square error.

4.4 Validation results

Figure 12 shows the validation results between the GCC SOS extracted by the PhenoCam GCC and the SOS extracted by the NASA VNP22Q2 product, USGS MCD12Q2 product, and the optimal parameters proposed (Figure 6 and Figure 9). As shown in Figure 12, the SOS results

extracted by optimal parameters had a higher accuracy than the NASA and USGS phenology products regardless of which phenology extraction method was used. Specifically, for the inflection point method, the SOS results (R^2: 0.70; RMSE: 18.99) extracted by optimal parameters with the filtering process (Figure 12 (c)) had a higher accuracy than those (R^2: 0.66; RMSE: 19.96) extracted by optimal parameters without the filtering process (Figure 12 (b)) and those (R^2: 0.58; RMSE: 21.44) extracted by the NASA VNP22Q2 product (Figure 12 (a)). Similarly, for the relative threshold method, using optimal parameters and the filtering process produced more accurate SOS results (R^2: 0.81; RMSE: 15.48) (Figure 12 (f)) than those (R^2: 0.74; RMSE: 18.20) extracted without the filtering process (Figure 12 (e)) and those (R^2: 0.67; RMSE: 20.97) extracted by the USGS MCD12Q2 product (Figure 12 (d)).

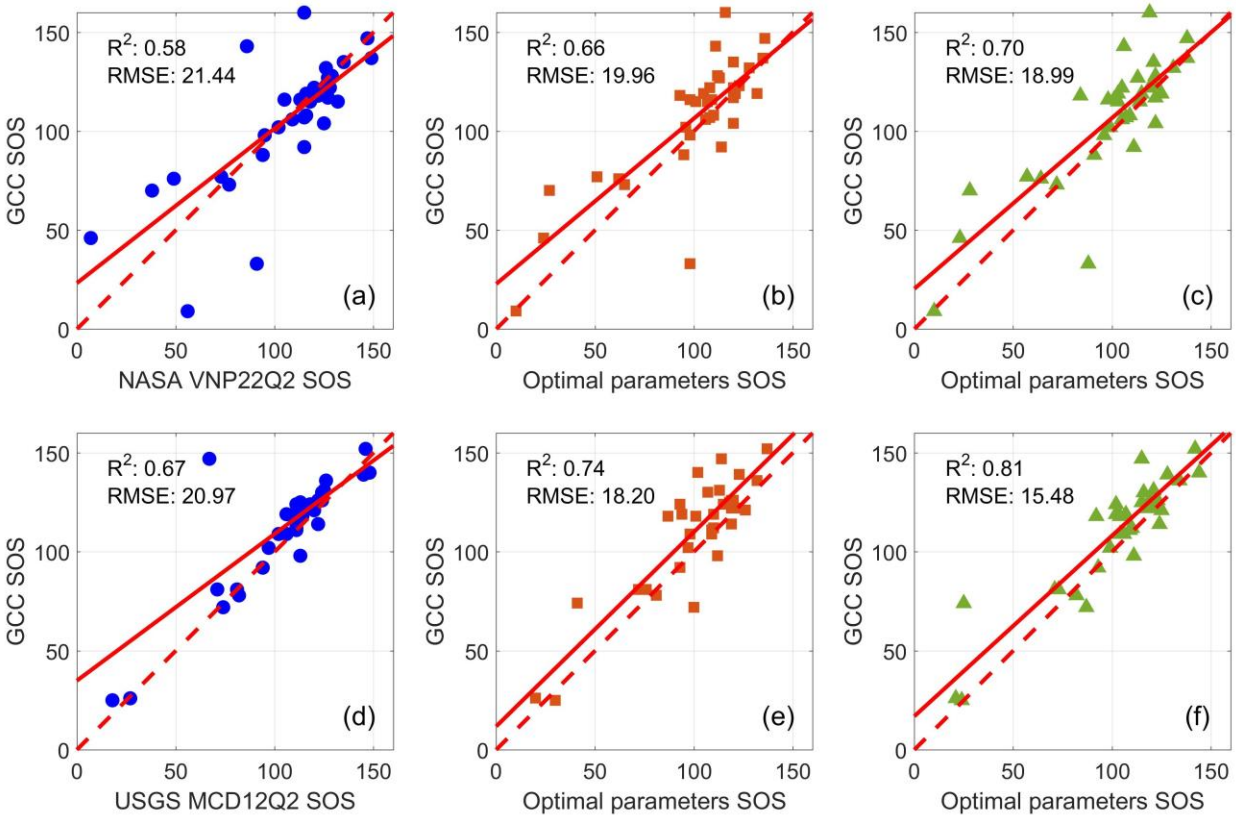

Figure 12. Scatterplots of the green chromatic coordinate (GCC) start of season (SOS) and the SOS extracted by the National Aeronautics and Space Administration (NASA) VNP22Q2 product (a), optimal parameters without the filtering process using the inflection point method (b), optimal parameters with the filtering process using the inflection point method (c), the United States Geological Survey (USGS) MCD12Q2 product (d), optimal parameters without the

filtering process using the relative threshold method (e), and optimal parameters with the filtering process using the relative threshold method (f).

5 Discussion

5.1 Soundness of the simulation data

We calculated the daily-average EVI time series of all non-sparse vegetation pixels over 20 years as EVI_{ref} in each 5° × 5° grid cell because: (1) various effects from cloud and snow contamination, sensor and solar angles, and land cover changes can be significantly excluded and (2) the average EVI profiles can represent a proxy for the vegetation growth and dynamic of each sub-region, which is widely used to improve the accuracy of phenology detection and analysis of phenological spatial patterns (Cong et al., 2012; Shen et al., 2016). In addition, the EVI_s time series were simulated by adding Gaussian noise (mean: 0; std: 0.02) and local cloud frequency effects into the EVI_{ref} of each grid cell (Figure 3), which is a common method to generate simulated VI time series (Cao et al., 2018, 2015). We further compared the simulated EVI time series and real EVI time series extracted by the MODIS MOD09GA products in 2018, as shown in Figure 13. The simulated EVI better captured the trajectory of the EVI time series in terms of the amplitude, width and range, and effectively simulated the fluctuations in all cases. The location information of the 12 pixels used is summarized in Table S2 in Appendix A. Supplementary data.

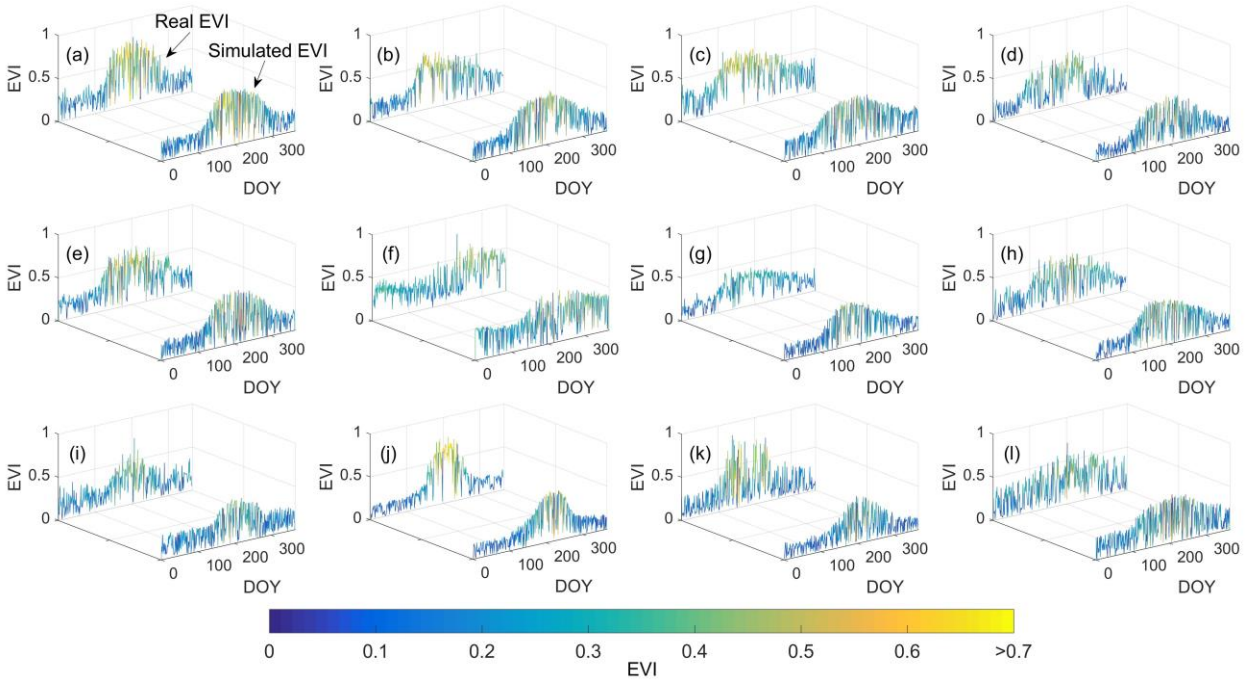

Figure 13. Comparison of the simulated enhanced vegetation index (EVI) time series and real EVI time series of 12 vegetation pixels (a)–(l) in 2018. DOY: day of year.

5.2 Effects of cloud coverage on SOS detection accuracy

To explore the effects of cloud coverage (Figure 2) on the SOS detection accuracy, we calculated the monthly-average cloudy days in each grid cell during the vegetation growth period (i.e., a period when the EVI increases from the minimum to the maximum), which is a crucial period for defining the SOS by the inflection point and relative threshold algorithms (Shang et al., 2017; Shen et al., 2014; Zhang et al., 2003). We then classified the cloud coverage situations into three levels, namely mild, moderate, and severe, by trisection of all of the grid cells (Figure S5 in Appendix A. Supplementary data). Meanwhile, we summarized the RMSE of the SOS (i.e., SOS accuracy) extracted by different composite periods using the inflection point and relative threshold algorithms, respectively (Figure 4). Because the filtering process will further remove the cloud noises in the MVC time series, we only investigated the effects of cloud coverage on the SOS detection accuracy without the filtering process (Figure 14). Figure 14 shows that cloud coverage has a greater effect on the SOS accuracy extracted by shorter composite periods (e.g., 3 and 5 days), i.e., more cloud coverage resulted in a lower SOS extraction accuracy for such periods regardless of which phenology extraction method was used. This is a possible reason

causing the lower SOS extraction accuracy (Figure 4) in higher latitude regions with frequent cloud coverage. However, more cloud coverage had little effect on SOS accuracy when using composite periods longer than or equal to 8 days for both phenology extraction methods (Figure 14), and less cloud coverage could even lower the SOS accuracy. One possible reason for this is that the EVI composites of shorter composite periods (e.g., 3 and 5 days) have more noisy effects from cloud coverage (Figure 3), which reduces the SOS detection accuracy. Moreover, although longer composite periods can weaken the negative fluctuations from cloud effects (Figure 3), the EVI profiles may be over-smoothed because of an excessive number of composite periods for regions with less cloud coverage, which results in a lower SOS extraction accuracy (Figure 14).

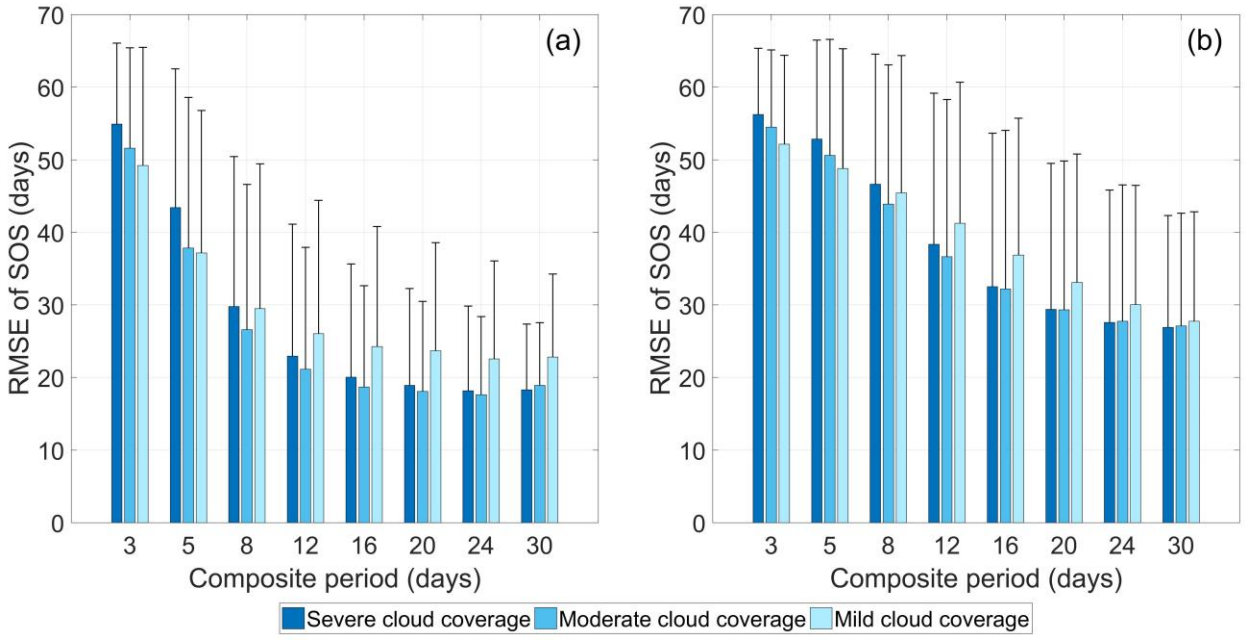

Figure 14. Relationship between the start of season (SOS) detection accuracy extracted by different composite periods and the cloud coverage levels in the vegetation growth period for (a) the inflection point method and (b) the relative threshold method. RMSE: root mean square error.

We further analyzed the relationship between the optimal composite periods without the filtering process (Figure 6) and the number of cloudy days during the vegetation growth period in each grid cell using the inflection point and relative threshold algorithms, respectively (Figure 15). The optimal composite periods are generally longer in regions with higher cloud frequency, thereby suggesting that longer MVC periods are needed in these regions to remove the more

serious cloud contamination. For grid cells with optimal composite periods longer than 16 days, the selection of optimal composite periods may not be solely determined by the cloud frequency. This may be because composite periods longer than 16 days (e.g., 20, 24, and 30 days) have similar abilities to remove clouds in the EVI time series, as shown in Figure 3 (c); thus, the accuracy of the SOS extraction may depend on other factors (e.g., the temporal interval of clear observations in a time series) (Zhang et al., 2009). In addition, because the inflection point phenology detection algorithm uses the logistic function to fit the time series, which can also remove noise, the optimal composite periods of the inflection point method are often shorter than those of the relative threshold method in regions with similar cloud effects. Another possible reason is that the inflection point method relies more on the shape of the EVI curves of the vegetation growth period, whereas the relative threshold method is more dependent on the values of the EVI curves. Thus, the inflection point method is more tolerant to the noise in the EVI curves, so it does not require a long composite period to completely remove noise.

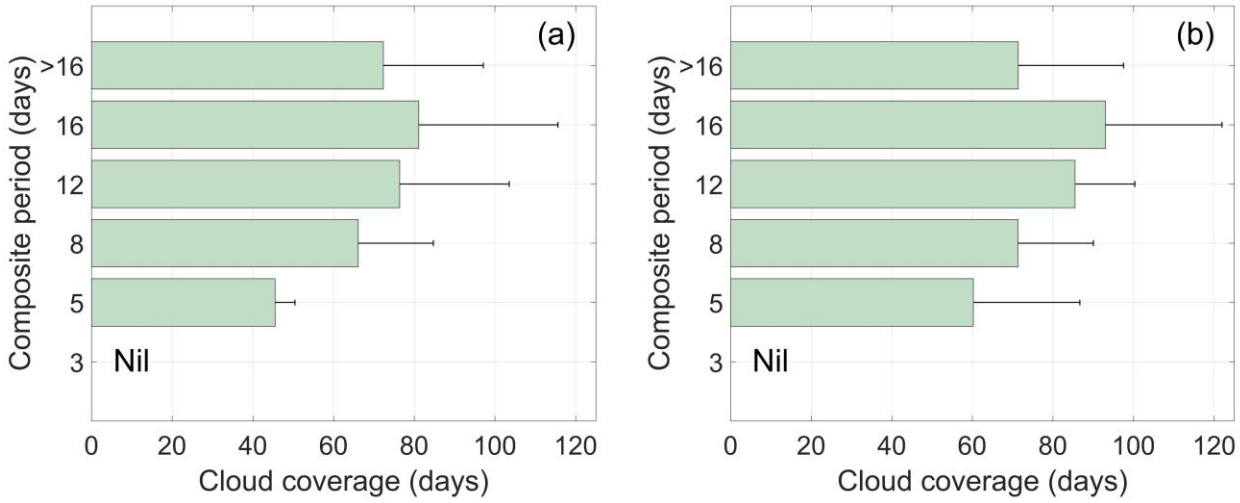

Figure 15. Relationship between the optimal composite periods and the number of cloudy days in the vegetation growth period for (a) the inflection point method and (b) the relative threshold method.

5.3 Implications for remote sensing phenology

Numerous studies (Fu et al., 2014; Gao et al., 2020; Shen et al., 2020; Wang and Zhu, 2019; Zhang et al., 2020) and official phenology products (e.g., VIIRS VNP22Q2 and MODIS MCD12Q2) have used global constant parameters of the MVC and smoothing filter to detect vegetation phenology regardless of the location of the study area. However, the constant parameter may cause the misconstruction of VI composites, which will further lead to misestimation of phenology metrics (Figure 4 and Figure 8). We found that the optimal parameters of the MVC and composite periods were clearly heterogeneous (Figure 6 and Figure 9), which implies that existing studies using a uniform composite period (Table 1) and official phenology products (VNP22Q2 and MCD12Q2) from NASA and USGS for phenology monitoring may have large errors in regions where the optimal composite period is very different from the uniform period. As errors of SOS detection from smoothing process are mainly systematic bias (Figure 5), suggesting that smoothing process of MVC and filters may not lead to large errors in interannual trends of SOS. However, this bias may lead to large errors if we study the large-scale spatial pattern of SOS because cloud frequencies change with regions. Furthermore, the findings shown in Figure 6 and Figure 9 also challenge the composite periods suggested by previous studies, such as 6 to 16 days (Zhang et al., 2009) or less than 28 days (Kross et al., 2011) on vegetation phenology detection. Thus, this study identified the optimal parameters of the MVC and smoothing filters using two simulation experiments with and without the filtering process. Finally, the optimal parameters of the MVC and smoothing filters were given in each grid cell, which may be beneficial for future studies on vegetation phenology to improve the accuracy of spring phenology detection from satellite-based VI time series in the northern hemisphere.

5.4 Limitations and future studies

This study has several limitations. First, the optimal parameters of the MVC and smoothing filters were based on each 5° × 5° grid cell over northern hemisphere (north of 30°) (Figure 2). Due to the regions with strong seasonality and observable phenological patterns, the northern hemisphere, particularly for the north of 30°, has been selected as the study area to investigate vegetation dynamics and phenology at large scales (Shen et al., 2020; Wang and Zhu, 2019).

Based on this, we selected the north of 30° as our region of interest to find optimal parameters of smoothing process in this study that may benefit many future studies. Also, the optimal parameters recommended in this study may be applicable to other regions out of north of 30° (e.g., southern hemisphere) if the vegetation has strong seasonality and the distribution of cloud cover is similar. However, the recommended optimal parameters may have slight differences for small-scale regions (e.g., a city) because of complex land surface cover and rapid cloud variation. Therefore, we suggest that preliminary work to identify optimal parameters is essential for phenology detection in small-scale studies. Second, although we only explored the optimal parameters of smoothing process for SOS extraction, the optimal parameters recommended can be also suitable for other phenological metrics, e.g., end of season (EOS) and length of season (LOS). For example, the longer composite periods of MVC are crucial to extract EOS and LOS in regions with higher cloud coverage. However, further studies are needed to investigate the best smoothing process for phenological metrics other than SOS. Third, owing to the high similarity of the satellite-based VI (e.g., NDVI, EVI, EVI2, and NDPI) time series, we selected the EVI as representative to identify the optimal parameters of the MVC and smoothing filters in this study. However, the usability of the optimal parameters (Figure 6 and Figure 9) for other VIs requires further exploration and analysis. Fourth, this study only investigated the two popular smoothing filters (i.e., SG and SP filters) used by NASA and the USGS. If inappropriate parameters of smoothing filters are used, over-smoothing or distortion of the VI profiles would have occur. Therefore, it is crucial to explore the optimal parameters of more smoothing filters and algorithms (e.g., Table 1) in future studies. Our study provides a prototype and framework for investigating how to assess the effects of satellite-based VI time series on SOS detection and how to identify optimal parameters of MVC and smoothing filters. Future studies on more VIs, phenological metrics, such as EOS and LOS, smoothing filter methods, and phenology extraction methods can assist in exploring this issue more thoroughly.

6 Conclusion

Many studies on vegetation phenology detection applied the MVC and smoothing filters with global constant parameters to preprocess the VI time series. However, we found that due to

variation in cloud cover conditions in regions over the northern hemisphere (north of 30°N) the globally constant parameters of the MVC and smoothing filters may result in misconstruction of the VI time series and further lead to errors in vegetation phenology detection. Accordingly, this study designed two simulation experiments to determine the optimal parameters of the MVC and smoothing filters in each 5° × 5° sub-region over the northern hemisphere. The MVC procedure, smoothing filters (SG and SP filters), and phenology extraction methods (inflection point and relative threshold methods) adopted by NASA and the USGS were analyzed. The results showed that the optimal parameters of both the MVC and smoothing filters had notable spatial heterogeneity, thereby suggesting that local optimal parameters of the MVC and smoothing filters should be used for detecting vegetation phenology metrics in the northern hemisphere from satellite VI time series, particularly for regions with diverse cloud frequencies, instead of using global uniform parameters. This study provides guidelines for future studies for setting appropriate parameters when using the MVC and filtering process to smooth VI time series for phenology detection and will benefit the generation of satellite phenology products on a large scale.

Acknowledgments

This study was supported by the National Natural Science Foundation of China (project No.42022060), the Research Institute for Sustainable Urban Development of the Hong Kong Polytechnic University (project No. 1-BBWD), and JSPS Grant-Aid for Scientific Research (C) (project No. 20K12146).

Appendix A. Supplementary data

Supplementary data to this article can be found online at: ######

References

Beurs, K.M. De, Henebry, G.M., 2004. Land surface phenology , climatic variation , and institutional change : Analyzing agricultural land cover change in Kazakhstan. Remote

Sensing of Environment 89, 497–509. https://doi.org/10.1016/j.rse.2003.11.006

Bórnez, K., Descals, A., Verger, A., Peñuelas, J., 2020. Land surface phenology from VEGETATION and PROBA-V data . Assessment over deciduous forests. Int J Appl Earth Obs Geoinformation 84, 101974. https://doi.org/10.1016/j.jag.2019.101974

Buitenwerf, R., Rose, L., Higgins, S.I., 2015. Three decades of multi-dimensional change in global leaf phenology. Nature Climate Change 5, 364–368. https://doi.org/10.1038/nclimate2533

Cao, R., Chen, J., Shen, M., Tang, Y., 2015. An improved logistic method for detecting spring vegetation phenology in grasslands from MODIS EVI time-series data. Agricultural and Forest Meteorology 200, 9–20. https://doi.org/10.1016/j.agrformet.2014.09.009

Cao, R., Chen, Y., Shen, M., Chen, J., Zhou, J., Wang, C., Yang, W., 2018. A simple method to improve the quality of NDVI time-series data by integrating spatiotemporal information with the Savitzky-Golay filter. Remote Sensing of Environment 217, 244–257. https://doi.org/10.1016/j.rse.2018.08.022

Chen, J., Jönsson, P., Tamura, M., Gu, Z., Matsushita, B., Eklundh, L., 2004. A simple method for reconstructing a high-quality NDVI time-series data set based on the Savitzky-Golay filter. Remote Sensing of Environment 91, 332–344. https://doi.org/10.1016/j.rse.2004.03.014

Cong, N., Piao, S., Chen, A., Wang, X., Lin, X., Chen, S., Han, S., Zhou, G., Zhang, X., 2012. Spring vegetation green-up date in China inferred from SPOT NDVI data: A multiple model analysis. Agricultural and Forest Meteorology 165, 104–113. https://doi.org/10.1016/j.agrformet.2012.06.009

Dallimer, M., Tang, Z., Bibby, P.R., Brindley, P., Gaston, K.J., Davies, Z.G., 2011. Temporal changes in greenspace in a highly urbanized region. Biology letters 763–766.

Delbart, N., Le, T., Kergoat, L., Fedotova, V., 2006. Remote sensing of spring phenology in boreal regions : A free of snow-effect method using NOAA-AVHRR and SPOT-VGT data (1982 – 2004). Remote Sensing of Environment 101, 52–62.

https://doi.org/10.1016/j.rse.2005.11.012

Fu, Y.H., Piao, S., Zhao, H., Jeong, S., 2014. Unexpected role of winter precipitation in determining heat requirement for spring vegetation green-up at northern middle and high latitudes. Global Change Biology 3743–3755. https://doi.org/10.1111/gcb.12610

Gao, M., Wang, X., Zhang, Y., Piao, S., Meng, F., Liu, Q., Li, X., 2020. Three-dimensional change in temperature sensitivity of northern vegetation phenology. Global Change Biology 5189–5201. https://doi.org/10.1111/gcb.15200

Giglio, L., Boschetti, L., Roy, D., Humber, M., Hall, J. V, 2018. Collection 6 MODIS Burned Area Product User ' s Guide Version 1 . 2 1–30.

He, Y., Lee, E., Warner, T.A., 2017. A time series of annual land use and land cover maps of China from 1982 to 2013 generated using AVHRR GIMMS NDVI3g data. Remote Sensing of Environment 199, 201–217. https://doi.org/10.1016/j.rse.2017.07.010

Holben, B.N., 1986. Characteristics of maximum-value composite images from temporal AVHRR data. International Journal of Remote Sensing 1161. https://doi.org/10.1080/01431168608948945

Huete, A., Didan, K., Miura, T., Rodriguez, E.P., Gao, X., Ferreira, L.G., 2002. Overview of the radiometric and biophysical performance of the MODIS vegetation indices. Remote Sensing of Environment 83. https://doi.org/10.1080/0965156x.2013.836857

Huete, A., Justice, C., Liu, H., 1994. Development of Vegetation and Soil Indices for MODIS-EOS. Remote Sensing of Environment 234, 224–234.

Jeong, S.J., Schimel, D., Frankenberg, C., Drewry, D.T., Fisher, J.B., Verma, M., Berry, J.A., Lee, J.E., Joiner, J., 2017. Application of satellite solar-induced chlorophyll fluorescence to understanding large-scale variations in vegetation phenology and function over northern high latitude forests. Remote Sensing of Environment 190, 178–187. https://doi.org/10.1016/j.rse.2016.11.021

Julien, Y., Sobrino, J.A., 2010. Comparison of cloud-reconstruction methods for time series of

composite NDVI data. Remote Sensing of Environment 114, 618–625. https://doi.org/10.1016/j.rse.2009.11.001

Keenan, T.F., Richardson, A.D., Hufkens, K., Keenan, T.F., 2020. On quantifying the apparent temperature sensitivity of plant phenology. New Phytologist 1033–1040. https://doi.org/10.1111/nph.16114

Kross, A., Fernandes, R., Seaquist, J., Beaubien, E., 2011. The effect of the temporal resolution of NDVI data on season onset dates and trends across Canadian broadleaf forests. Remote Sensing of Environment 115, 1564–1575. https://doi.org/10.1016/j.rse.2011.02.015

Maisongrande, Duchemin, Dedieu, 2004. VEGETATION / SPOT : an operational mission for the Earth monitoring ; presentation of new standard products. International Journal of Remote Sensing 1161. https://doi.org/10.1080/0143116031000115265

Meng, L., Mao, J., Zhou, Y., Richardson, A.D., Lee, X., Thornton, P.E., 2020. Urban warming advances spring phenology but reduces the response of phenology to temperMeng, L., Mao, J., Zhou, Y., Richardson, A.D., Lee, X., Thornton, P.E., 2020. Urban warming advances spring phenology but reduces the response of phenology to temperatu. Proceedings of the National Academy of Sciences of the United States of America 2–7. https://doi.org/10.1073/pnas.1911117117

Moon, M., Li, D., Liao, W., Rigden, A.J., Friedl, M.A., 2020. Modification of surface energy balance during springtime : The relative importance of biophysical and meteorological changes. Agricultural and Forest Meteorology 284, 107905. https://doi.org/10.1016/j.agrformet.2020.107905

Moon, M., Zhang, X., Henebry, G.M., Liu, L., Gray, J.M., Melaas, E.K., Friedl, M.A., 2019. Long-term continuity in land surface phenology measurements : A comparative assessment of the MODIS land cover dynamics and VIIRS land surface phenology products. Remote Sensing of Environment 226, 74–92. https://doi.org/10.1016/j.rse.2019.03.034

Motohka, T., Agency, E., Nasahara, K., Murakami, K., 2011. Evaluation of Sub-Pixel Cloud Noises on MODIS Daily Spectral Indices Based on in situ Measurements. Remote Sensing.

https://doi.org/10.3390/rs3081644

Myneni, R.B., Keelingt, C.D., Tucker, C.J., Asrar, G., 1997. Increased plant growth in the northern high latitudes from 1981 to 1991. Nature 386, 1–5.

Reed, B.C., Brown, J.F., VanderZee, D., Loveland, T.R., Merchant, J.W., Ohlen, D.O., 1994. Measuring phenological variability from satellite imagery. Journal of vegetation science 5, 703–714.

Savitzky, A., Golay, M.J., 1964. Smoothing and differentiation of data by simplified least squares procedures. Analytical chemistry 36, 1627–1639.

Shang, R., Liu, R., Xu, M., Liu, Y., Zuo, L., Ge, Q., 2017. The relationship between threshold-based and inflexion-based approaches for extraction of land surface phenology. Remote Sensing of Environment 199, 167–170. https://doi.org/10.1016/j.rse.2017.07.020

Shen, M., Jiang, N., Peng, D., Rao, Y., Huang, Y., 2020. Can changes in autumn phenology facilitate earlier green-up date of northern vegetation ? Agricultural and Forest Meteorology 291, 108077. https://doi.org/10.1016/j.agrformet.2020.108077

Shen, M., Piao, S., Chen, X., An, S., Fu, Y.H., Wang, S., Cong, N., Janssens, I.A., 2016. Strong impacts of daily minimum temperature on the green-up date and summer greenness of the Tibetan Plateau. Global change biology 22, 3057–3066. https://doi.org/10.1111/gcb.13301

Shen, M., Zhang, G., Cong, N., Wang, S., Kong, W., Piao, S., 2014. Increasing altitudinal gradient of spring vegetation phenology during the last decade on the Qinghai-Tibetan Plateau. Agricultural and Forest Meteorology 189–190, 71–80. https://doi.org/10.1016/j.agrformet.2014.01.003

Verma, M., Friedl, M.A., Finzi, A., Phillips, N., 2016. Multi-criteria evaluation of the suitability of growth functions for modeling remotely sensed phenology. Ecological Modelling 323, 123–132. https://doi.org/10.1016/j.ecolmodel.2015.12.005

Vrieling, A., Meroni, M., Darvishzadeh, R., Skidmore, A.K., Wang, T., Zurita-milla, R., Oosterbeek, K., Connor, B.O., Paganini, M., 2019. Vegetation phenology from Sentinel-2

and field cameras for a Dutch barrier island. Remote Sensing of Environment 215, 517–529. https://doi.org/10.1016/j.rse.2018.03.014

Wang, C., Chen, J., Wu, J., Tang, Y., Shi, P., Black, T.A., Zhu, K., 2017. A snow-free vegetation index for improved monitoring of vegetation spring green-up date in deciduous ecosystems. Remote Sensing of Environment 196, 1–12. https://doi.org/10.1016/j.rse.2017.04.031

Wang, C., Zhu, K., 2019. Misestimation of Growing Season Length Due to Inaccurate Construction of Satellite Vegetation Index Time Series. IEEE Geoscience and Remote Sensing Letters 16, 1185–1189. https://doi.org/10.1109/LGRS.2019.2895805

Wang, J., Zhang, X., 2020. Investigation of wildfire impacts on land surface phenology from MODIS time series in the western US forests. ISPRS Journal of Photogrammetry and Remote Sensing 159, 281–295. https://doi.org/10.1016/j.isprsjprs.2019.11.027

Wang, S., Ju, W., Peñuelas, J., Cescatti, A., Zhou, Y., Fu, Y., Huete, A., Liu, M., Zhang, Y., 2019. Urban−rural gradients reveal joint control of elevated CO2 and temperature on extended photosynthetic seasons. Nature Ecology & Evolution 3. https://doi.org/10.1038/s41559-019-0931-1

White, M.A., de Beurs, K.M., Didan, K., Inouye, D.W., Richardson, A.D., Jensen, O.P., O'Keefe, J., Zhang, G., Nemani, R.R., van Leeuwen, W.J.D., Brown, J.F., de Wit, A., Schaepman, M., Lin, X., Dettinger, M., Bailey, A.S., Kimball, J., Schwartz, M.D., Baldocchi, D.D., Lee, J.T., Lauenroth, W.K., 2009. Intercomparison, interpretation, and assessment of spring phenology in North America estimated from remote sensing for 1982-2006. Global Change Biology 15, 2335–2359. https://doi.org/10.1111/j.1365-2486.2009.01910.x

Wickham, H., Hofmann, H., Wickham, C., Cook, D., Wiley, J., 2012. Glyph-maps for visually exploring temporal patterns in climate data and models †. Environmetrics 382–393. https://doi.org/10.1002/env.2152

Wilson, A.M., Jetz, W., 2016. Remotely Sensed High-Resolution Global Cloud Dynamics for Predicting Ecosystem and Biodiversity Distributions. PLOS Biology 1–20. https://doi.org/10.1371/journal.pbio.1002415

867 Xu, S., Yu, Z., Lettenmaier, D.P., Mcvicar, T.R., Ji, X., 2020. Elevation-dependent response of
868 vegetation dynamics to climate change in a cold mountainous region OPEN ACCESS
869 Elevation-dependent response of vegetation dynamics to climate change in a cold
870 mountainous region. Environmental Research Letters.

871 Yu, H., Luedeling, E., Xu, J., 2010. Winter and spring warming result in delayed spring
872 phenology on the Tibetan Plateau. Proceedings of the National Academy of Sciences 107,
873 22151–22156. https://doi.org/10.1073/pnas.1012490107

874 Zeng, L., Wardlow, B.D., Xiang, D., Hu, S., Li, D., 2020. A review of vegetation phenological
875 metrics extraction using time-series , multispectral satellite data. Remote Sensing of
876 Environment 237, 111511. https://doi.org/10.1016/j.rse.2019.111511

877 Zhang, J., Zhao, J., Wang, Y., Zhang, H., Zhang, Z., 2020. Comparison of land surface
878 phenology in the Northern Hemisphere based on AVHRR GIMMS3g and MODIS datasets.
879 ISPRS Journal of Photogrammetry and Remote Sensing 169, 1–16.
880 https://doi.org/10.1016/j.isprsjprs.2020.08.020

881 Zhang, X., 2015. Reconstruction of a complete global time series of daily vegetation index
882 trajectory from long-term AVHRR data. Remote Sensing of Environment 156, 457–472.
883 https://doi.org/10.1016/j.rse.2014.10.012

884 Zhang, X., Friedl, M.A., Schaaf, C.B., 2009. Sensitivity of vegetation phenology detection to the
885 temporal resolution of satellite data. International Journal of Remote Sensing 30, 2061–
886 2074. https://doi.org/10.1080/01431160802549237

887 Zhang, X., Friedl, M.A., Schaaf, C.B., Strahler, A.H., Hodges, J.C., Gao, F., Reed, B.C., Huete,
888 A., 2003. Monitoring vegetation phenology using MODIS. Remote sensing of environment
889 84, 471–475.

890 Zhang, X., Liu, L., Liu, Y., Jayavelu, S., Wang, J., Moon, M., Henebry, M., Friedl, M.A., Schaaf,
891 C.B., 2018. Generation and evaluation of the VIIRS land surface phenology product.
892 Remote Sensing of Environment 216, 212–229. https://doi.org/10.1016/j.rse.2018.06.047

893 Zhang, X., Liu, L., Yan, D., 2017a. Comparisons of global land surface seasonality and

phenology derived from AVHRR, MODIS, and VIIRS data. Journal of Geophysical Research: Biogeosciences 1506–1525. https://doi.org/10.1002/2017JG003811

Zhang, X., Wang, J., Gao, F., Liu, Y., Schaaf, C., Friedl, M., Yu, Y., Jayavelu, S., Gray, J., Liu, L., Yan, D., Henebry, G.M., 2017b. Exploration of scaling effects on coarse resolution land surface phenology. Remote Sensing of Environment 190, 318–330. https://doi.org/10.1016/j.rse.2017.01.001

Zhou, D., Zhao, S., Zhang, L., Liu, S., 2016. Remotely sensed assessment of urbanization effects on vegetation phenology in China's 32 major cities. Remote Sensing of Environment 176, 272–281. https://doi.org/10.1016/j.rse.2016.02.010

Zhu, Y., Zhang, Y., Zu, J., Wang, Z., Huang, K., Cong, N., Tang, Z., 2019. Effects of data temporal resolution on phenology extractions from the alpine grasslands of the Tibetan Plateau. Ecological Indicators 104, 365–377. https://doi.org/10.1016/j.ecolind.2019.05.004

Zu, J., Zhang, Y., Huang, K., Liu, Y., Chen, N., Cong, N., 2018. Biological and climate factors co-regulated spatial-temporal dynamics of vegetation autumn phenology on the Tibetan Plateau. Int J Appl Earth Obs Geoinformation 69, 198–205. https://doi.org/10.1016/j.jag.2018.03.006